

AD-A236 351



GL-TR-90-0286

ARC-TR-90-010

2

Limb Retrieval Capability of the Spirit 3 Radiometer

A. S. Zachor

Atmospheric Radiation Consultants, Inc.
59 High Street
Acton, MA 01720

17 August 1990

Scientific Report No. 5

DTIC
ELECTE
MAY 31 1991
S B D

APPROVED FOR PUBLIC RELEASE; DISTRIBUTION UNLIMITED

GEOPHYSICS LABORATORY
AIR FORCE SYSTEMS COMMAND
UNITED STATES AIR FORCE
HANSCOM AIR FORCE BASE, MASSACHUSETTS 01731-5000

91-00781



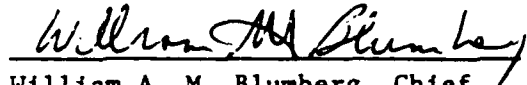
91 5 29

177

This technical report has been reviewed and is approved for publication.



DEAN F. KIMBALL
Contract Manager
Simulation Branch



William A. M. Blumberg, Chief
Simulation Branch
Optical Environment Division



R. EARL GOOD, SES, Director
Optical Environment Division

This document has been reviewed by the ESD Public Affairs Office(PA) and is releasable to the National Technical Information Service (NTIS).

Qualified requestors may obtain additional copies from the Defense Technical Information Center. All others should apply to the National Technical Information Service.

If your address has changed, or if you wish to be removed from the mailing list, or if the addressee is no longer employed by your organization, please notify PL/IMA, Hanscom AFB, MA 01731-5000. This will assist us in maintaining a current mailing list.

Do not return copies of this report unless contractual obligations or notices on a specific document requires that it be returned.

REPORT DOCUMENTATION PAGE

DATE: 17 AUG 1990

1. AGENCY USE ONLY (Leave blank)		2. REPORT DATE 17 August 1990		3. REPORT TYPE AND DATES COVERED Scientific No. 5	
4. TITLE AND SUBTITLE Limb Retrieval Capability of the Spirit 3 Radiometer				5. FUNDING NUMBERS PE 63220C PR S321 TA 22 WU AA Contract F19628-87-C-0130	
6. AUTHOR(S) Alexander S. Zachor					
7. PERFORMING ORGANIZATION NAME(S) AND ADDRESS(ES) Atmospheric Radiation Consultants, Inc. 59 High Street Acton, MA 01720				8. PERFORMING ORGANIZATION REPORT NUMBER ARC-TR-90-010	
9. SPONSORING MONITORING AGENCY NAME(S) AND ADDRESS(ES) Geophysics Laboratory Hanscom AFB, MA 01731-5000 Contract Manager: Dean Kimball/OPB				10. SPONSORING MONITORING AGENCY REPORT NUMBER GL-TR-90-0286	
11. SUPPLEMENTARY NOTES					
12a. DISTRIBUTION AVAILABILITY STATEMENT APPROVED FOR PUBLIC RELEASE; DISTRIBUTION UNLIMITED				12b. DISTRIBUTION CODE	
13. ABSTRACT (Maximum 200 words) Noise levels were predicted as a function of tangent height for limb radiance profiles that will be measured by the SPIRIT 3 radiometer. Synthetic data was inverted to quantify the corresponding uncertainties in retrieved volume emission rates, and to quantify expected errors due to horizontal variations in atmospheric density. A new computer routine for derivative-free Abel inversion is described.					
14. SUBJECT TERMS Limb radiance profiles Limb retrieval Abel transform				15. NUMBER OF PAGES 72 16. PRICE CODE	
17. SECURITY CLASSIFICATION OF REPORT Unclassified		18. SECURITY CLASSIFICATION OF THIS PAGE Unclassified		19. SECURITY CLASSIFICATION OF ABSTRACT Unclassified	
				20. LIMITATION OF ABSTRACT SAR	

PREFACE

The work described herein was performed for Spectral Sciences, Inc. under Subcontract No. SSI-A-2184-02, which was funded by prime Contract No. F19628-87-C-0130 from the U.S. Air Force Systems Command. The author wishes to thank Dr. Robert O'Neil of GL/OPE and Dr. A. T. Stair, Jr. of ATSA for their expert guidance of the effort, and Dr. Clair Wyatt of SDL, Drs. Rob Sundberg, John Duff and John Gruninger of SSI and Dr. Harold Gardiner of GL/OPE for helpful discussions.



Accession For	
NTIS GRA&I	<input checked="" type="checkbox"/>
DTIC TAB	<input type="checkbox"/>
Unannounced	<input type="checkbox"/>
Justification	
By _____	
Distribution/	
Availability Codes	
Dist	Avail and/or Special
A-1	

TABLE OF CONTENTS

	<u>Page</u>
1. INTRODUCTION	1
2. NEW INVERSION ROUTINE FOR THE OPTICALLY-THIN CASE	3
3. MSX LIMB RETRIEVAL ISSUES	4
3.1 Limb-View Versus Zenith-View Retrieval Errors	4
3.2 Effects of Horizontal Density Variations . .	8
3.2.1 Retrieval Error for Case A	10
3.2.2 Retrieval Error for Case B	13
3.2.3 Retrieval Error for Case C	13
3.2.4 Summary	13
4. CYBER VERSION OF THE SHARC CODE	20
5. PERFORMANCE PREDICTIONS FOR THE SPIRIT 3 RADIOMETER BANDS	21
5.1 Predicted Uncertainty in Measured Limb Radiance Profiles	21
5.2 Predicted Uncertainty in Retrieved Volume Emission Rate Profiles	33
6. CONCLUSIONS	51
APPENDIX A ROUTINES FOR THE ABEL TRANSFORM AND ITS INVERSE	54
APPENDIX B FILES AND EXECUTION PROCEDURES FOR THE CYBER VERSION OF THE SHARC CODE	59
REFERENCES	64

LIST OF FIGURES

<u>Figure</u>		<u>Page</u>
1	Model density profile and relative errors in the density profile recovered by limb- view and zenith-view retrievals	5
2	Comparison of limb radiance profile and zenith- view radiance profile for the model density profile of Fig. 1	7
3	Effects of horizontal variations in remote limb sounding; general considerations	9
4	Modelling procedure used to study effects of horizontal density variations	11
5	Horizontal density variations for Case A	12
6	Recovered density profile for Case A and the density profile $n(H,0)$	14
7	Horizontal density variation for Case B	15
8	Recovered density profile for Case B and the density profile $n(H,0)$	16
9	Horizontal density variation for Case C	17
10	Recovered density profile for Case C and the density profile $n(H,0)$	18
11	Limb radiance profile and expected rms uncertainty in the measured limb radiance for Band D, Case 0	29
12	Same as Fig. 11, except the results represent Case 1	31
13	Same as Fig. 11, except the results represent Case 2	32
14	Same as Fig. 11, except the results represent Band E, Case 0	34
15	Same as Fig. 11, except the results represent Band E, Case 1	35
16	Same as Fig. 11, except the results represent Band E, Case 2	36

LIST OF FIGURES (Continued)

<u>Figure</u>		<u>Page</u>
17	Same as Fig. 11, except the results represent Band A, Case 0	37
18	Same as Fig. 11, except the results represent Band A, Case 1	38
19	Same as Fig. 11, except the results represent Band A, Case 2	39
20	The "true" vertical profile of volume emission, a typical retrieved profile, and the predicted rms error in the retrieved profile; for Band D, Case 1 and no smoothing	40
21	Same as Fig. 20, except the noisy limb radiance profile was smoothed once before the inversion .	43
22	Same as Fig. 20, except the results represent Case 2	45
23	Same as Fig. 20, except the results represent Band E, Case 2	46
24	Same as Fig. 23, except $NSMTH = 1$	47
25	Same as Fig. 20, except the results represent Band E, Case 2	48
26	Same as Fig. 20, except the results represent Band A, Case 1	49
27	Same as Fig. 20, except the results represent Band A, Case 2	50

LIST OF TABLES

<u>Table</u>	<u>Page</u>
1 SPIRIT-3 Radiometer Bands	24
2 SPIRIT 3 Earth Limb Mode Dynamic Performance for Band E -- from Eqs. (1-4)	24
3 Gain Switching Cases	26
B.1 Listing of Tape CC0888 (Edited RECLAIM Listing) .	59
B.2 Renamed SHARC Files	63

SECTION 1

INTRODUCTION

The research described in this final report was performed in support of the MSX project, specifically the SPIRIT 3 radiometer operating in the earth limb mode. Several issues relative to the capability of SPIRIT 3 to provide precise measurements of the earth limb IR background, as well as valid inferences of species volume emission rate profiles, were addressed. The effort attempted to answer these questions:

1.) Would the launch of a rocket-borne instrument that observed zenith radiances over its flight during the MSX mission significantly enhance the value of the SPIRIT 3 limb radiance measurements? The instrument could possibly obtain some *in situ* data in addition to the radiometric measurements.

2.) What are the errors in vertical profiles inferred from limb radiance data due to horizontal variations (departures from circular symmetry) in species densities or temperature?

3.) Given the particulars of the SPIRIT 3 dynamic performance, ie., a prescription for calculating total system noise, what are the expected noise levels vs. tangent height? The answer requires a prediction of the limb radiance profile and the history of radiance levels observed by the detectors during a limb scan (because of photon noise and the automatic gain ranging used by SPIRIT 3).

4.) From this noise analysis, what is the predicted uncertainty in the vertical profiles of species density (volume emission rate) obtained by inversion of the data? The answer is dependent on the particular inversion algorithm used to process the data.

Our effort on the first question was confined to determining the relative sensitivities required for zenith-viewing and limb-viewing radiometers to recover a vertical profile of volume emission rate to the same precision. Questions 1 and 2 are addressed in Section 3.

In dealing with Questions 1 and 4 it was necessary to invert synthetic limb radiance data and quantify the effects of noise propagation in the inversion procedure. For this purpose we developed a new, very stable, inversion algorithm based on a derivative-free form of the inverse Abel equation. The algorithm is described in Section 2.

Synthetic limb radiance profiles for the SPIRIT 3 radiometer bands were provided by GL. These were computed using the SHARC code. We made extensive changes to the SHARC Fortran coding to obtain a version that can be run on the Cyber computer at GL; the Cyber version of SHARC is described in Section 4.

Much of the study effort was devoted to Questions 3 and 4. The results, given in Section 5, represent a fairly comprehensive assessment of the expected performance of the SPIRIT 3 radiometer in Bands D, E and A.

SECTION 2

NEW INVERSION ROUTINE FOR THE OPTICALLY-THIN CASE

One of the objectives of this research is to quantify retrieval errors corresponding to expected noise levels for the SPIRIT 3 limb radiance data. This was accomplished by inverting synthetic limb radiance data with and without noise. Since we assume the optically thin case, the synthetic limb radiance profile can be computed by numerically evaluating the Abel integral equation for a given vertical profile of volume emission rate. Given a limb radiance profile, representing actual or synthetic data, one can recover the emission rate profile by evaluating the inverse Abel integral equation. For the purpose of carrying out this retrieval we developed a new subroutine based on an alternative form of the inverse Abel equation, given by *Deutsch and Beniaminy* [1982]. It does not require any derivatives of the limb radiance profile and hence is much less sensitive to noise in this profile than the more familiar form of the inverse Abel equation. We obtained the exact solution of the derivative-free integral for the case of a piecewise linear limb radiance profile (linearly connected sampled). This solution was coded to obtain the subroutine.

We also coded a subroutine to generate a synthetic limb radiance profile from the direct Abel equation. It evaluates an exact solution for a piecewise linear emission rate profile. The direct and inverse solutions (results of evaluating the integrals) are given in Appendix A. Also given are Fortran listings for the two subroutines.

The sensitivity of the new inversion routine to noise, as compared to other stable procedures for inverting Abel's equation, is discussed briefly in the Conclusions section.

SECTION 3

MSX LIMB RETRIEVAL ISSUES

This section addresses two issues of concern in the MSX program. One relates to the capability of a rocket-borne instrument package to provide data that would complement the MSX limb radiance measurements, ie., to provide a check on the limb inversion results, and/or to enable the retrieval of vertical profiles that cannot be recovered from the limb radiance data alone. The work reported here is limited to a comparison of sensitivities required when the same vertical profile is recovered from a.) the zenith radiance measured as a function of altitude, and b.) a limb radiance profile. The other, related issue is the effect of horizontal variations in volume emission rate on the vertical profiles obtained by limb inversion. The real atmosphere is not one-dimensional (spherically symmetric) as assumed by nearly all limb inversion techniques. We will demonstrate that the resulting limb retrieval errors are small.

3.1 Limb-View Versus Zenith-View Retrieval Errors

Our analysis of these errors is based on the density (volume emission rate) profile shown by the long-dashed curve in Fig. 1. This distribution is similar to an excited NO profile inferred from SPIRE data [Zachor, et al, 1985]. We computed the corresponding limb radiance profile and added Gaussian noise with a standard deviation equivalent to a signal-to-noise ratio (SNR) of 100 at the maximum of the limb radiance profile (the standard deviation was the same for all tangent heights). We then inverted the noise-contaminated limb radiance profile to obtain the solution (the retrieved density profile) shown by the solid curve in Fig. 1. We performed 250 such inversions, using a different noise set for each, and from the results calculated the rms

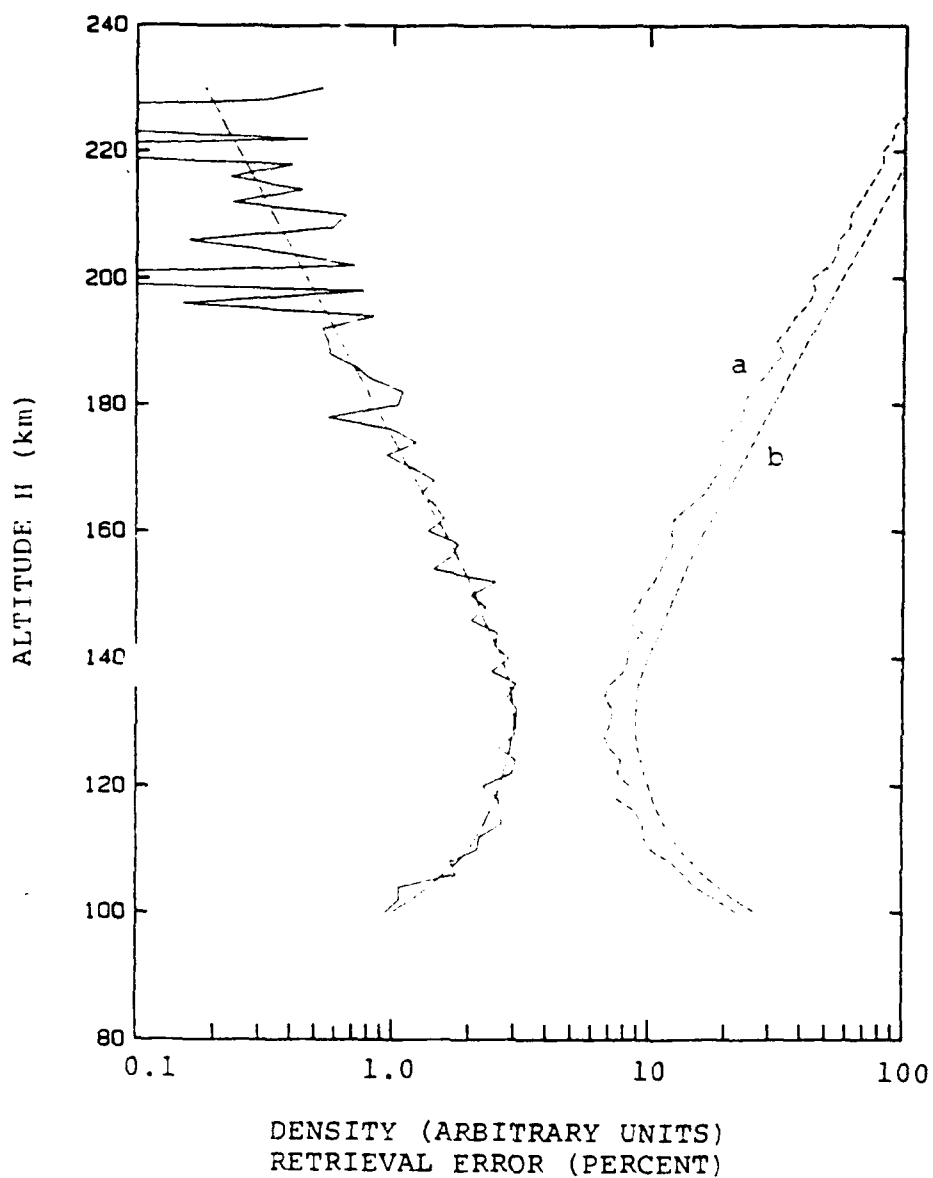


Fig. 1. Model density profile (long-dashed) curve, and a typical profile recovered by limb retrieval for $(S/N)_{MAX} = 100$ (solid curve). Rms relative error for 250 limb retrievals with $(S/N)_{MAX} = 100$ (curve a). Curve b gives the theoretical rms relative error for a zenith-viewing rocket experiment with 100 times greater sensitivity; the zenith-view $(S/N)_{MAX}$ is 420.

relative error in retrieved density as a function of altitude. This relative error profile is curve (a) in Fig. 1. The jagged features in the curve correspond to the statistical uncertainty in our estimate of the error (which resulted from using only 250 trials). The shape of the curve clearly indicates that the relative error is inversely proportional to the density, i.e., the error is independent of density (or altitude). The relative error below 170 km is 20 percent or less; at the peak of the NO* density profile near 130 km it is only seven percent. The error could be reduced considerably by smoothing the noisy data and/or the solution profile if two-kilometer vertical resolution is not required; this is the spacing of the samples for all profiles in Fig. 1. From computations performed for a wide range of SNR values, we established that the error scales directly with the noise level.

The vertical density profile can be recovered as -1 times the altitude derivative d/dH of the zenith radiance observed by a rocket-borne radiometer. The corresponding relative error in recovered density for a given system noise equivalent radiance (NER) and vertical sampling interval is expressible by a simple formula. Curve (b) in Fig. 1 shows the predicted relative error when the rocket instrument has an NER 100 times smaller than that of the limb-viewing sensor. Here again, the unnormalized error is independent of density or altitude, and scales directly with the noise level. The maximum radiance for the zenith-viewing sensor, i.e., the radiance at 100 km, is 24 times less than the maximum limb radiance. Thus, the maximum SNR is approximately 420 (equal to $100 \times 100/24$) compared to 100 for the limb-viewing case. Figure 2 compares the limb radiance profile and corresponding zenith radiance profile. Above 160 km, where the two profiles fall off exponentially, the limb is 35 times brighter than the zenith, for our model NO* profile.

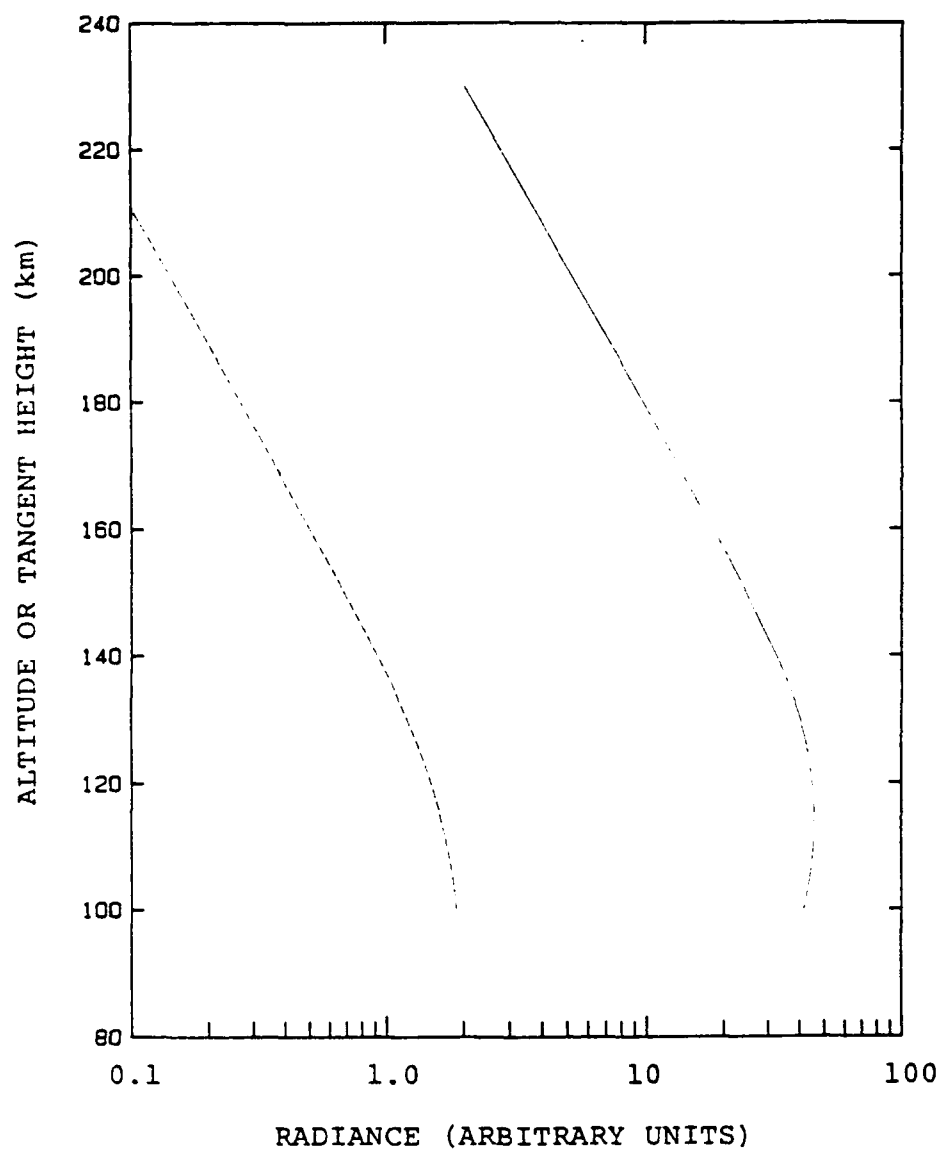


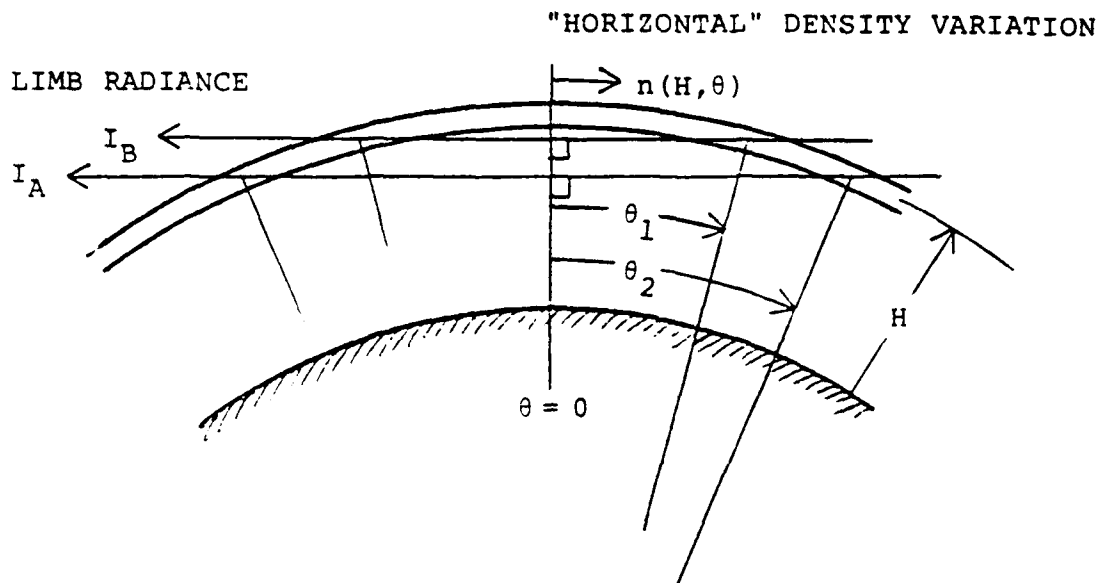
Fig. 2. Comparison of limb radiance profile (solid curve) and zenith-view radiance profile (dashed curve) for the model density profile of Fig. 1.

We conclude that the rocket instrument must have 100 times greater sensitivity (or achieve 4.2 times higher SNR) than the limb-viewing instrument in order to recover the model density profile to comparable accuracy. Of course, the rocket instrument can use a much larger IFOV to realize the higher sensitivity for a given detector NEP.

3.2 Effects of Horizontal Density Variations

The Abel inversion, like most other limb retrieval techniques, assumes a one-dimensional, or circularly-symmetric atmosphere. The vertical profiles recovered by these methods contain error when the actual atmospheric density varies "horizontally" as well as vertically. The following general considerations indicate that the error will be relatively small. They also suggest a simple functional form for modelling a horizontal density variation when the purpose is to evaluate its effect on the retrieved vertical profile.

Figure 3 defines the coordinates H and θ of a two-dimensional atmospheric density profile $n(H, \theta)$. The function $n(H, \theta)$ versus θ for fixed H can be decomposed into its even and odd parts. A moments thought will confirm that the odd part has no effect on the observed limb radiance profile: In the optically thin case, the odd part corresponds to equal-magnitude, opposite-sign contributions from the two segments of the limb path that traverse the same atmospheric layer (Fig. 3). Moreover, if $n(H, \theta)$ has a continuous derivative $d/d\theta$, then the derivative $d/d\theta$ of the even part will be zero at $\theta = 0$. In other words, for any plausible $n(H, \theta)$, the limb radiance contribution of the atmospheric layer at the tangent height is virtually unaffected by the horizontal density variation; this layer contributes more than any other layer to the observed radiance. In particular, any distribution $n(H, \theta)$ for which



$n(H, \theta)$ vs. θ = EVEN part + ODD part

FOR OPTICALLY-THIN CASE,

- a.) ODD part has no effect on $I(H_T)$ vs. H_T
- b.) $\frac{d}{d\theta}$ (EVEN part) = 0 at $\theta = 0$ for "smooth" $n(H, \theta)$
- c.) Linear $n(H, \theta)$ vs. θ gives same $I(H_T)$ as
 $n(H, \theta) = n(H, 0)$; limb sounding recovers $n(H, 0)$

Fig. 3. Effects of horizontal variations in remote limb sounding; general considerations.

$n(H, \theta)$ vs. θ is linear for all H results in the same limb radiance profile as $n(H, 0)$; limb sounding recovers the density profile $n(H, 0)$.

Based on the above argument it is reasonable to model the horizontal or θ -variation in $n(H, \theta)$ by a quadratic function. Figure 4 shows that we need only define the function between approximately -15 degrees and 15 degrees if we wish to recover the density between 100 and 200 km, and if we can assume the atmosphere above 300 km has virtually no effect on the result. Specifically, the modelling procedure consisted of choosing two different vertical density profiles, one for $\theta = 0$ and the other for $\theta = 15$ degrees, and performing quadratic interpolation to obtain $n(H, \theta)$ for any angle θ between 0 and 15 degrees. The interpolation formula that we used is

$$n(H, \theta) = [1 - W(\theta)]n_A(H) + W(\theta)n_B(H); \quad W(\theta) = (\theta/15^\circ)^2$$

where $n_A = n(H, 0)$ and $n_B = n(H, 15^\circ)$ are the selected density profiles for 0 and 15 degrees.

3.2.1 Retrieval error for Case A.

The density profile for $\theta = 0$ is the one shown in Fig. 1. For $\theta = 15$ degrees we used one that corresponds to a 5.3- μm NO cooling rate profile given by Gordiets, et al [1982]; the cooling rate is proportional to the profile of NO^* density. The two model density profiles, as well as interpolated profiles for $\theta = 5$ degrees and 10 degrees, are shown in Fig. 5. Note that $n(H, \theta)$ vs. θ is a maximum at $\theta = 0$ for H less 190 km, and that the horizontal variation over the portion of the limb path below 200 km ($\theta < 10$ deg) is 50 percent or greater within layers below 130 km.

We computed a noise-free limb radiance profile corresponding to this $n(H, \theta)$ distribution, and then inverted

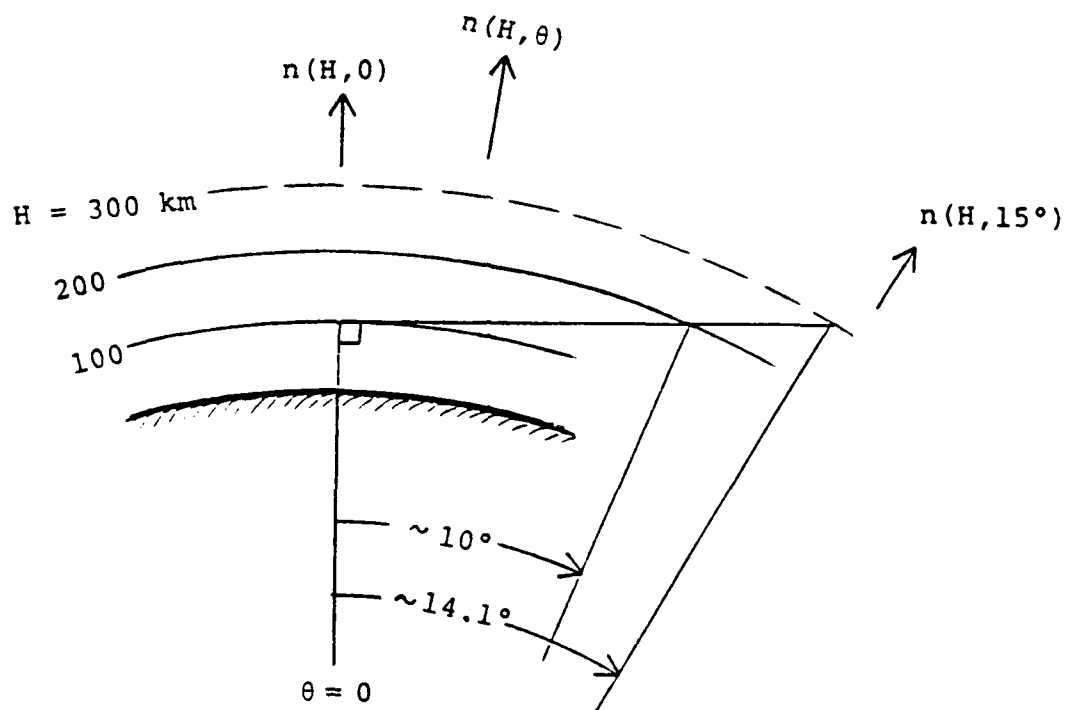


Fig. 4. Modelling procedure used to study effects of horizontal density variations.

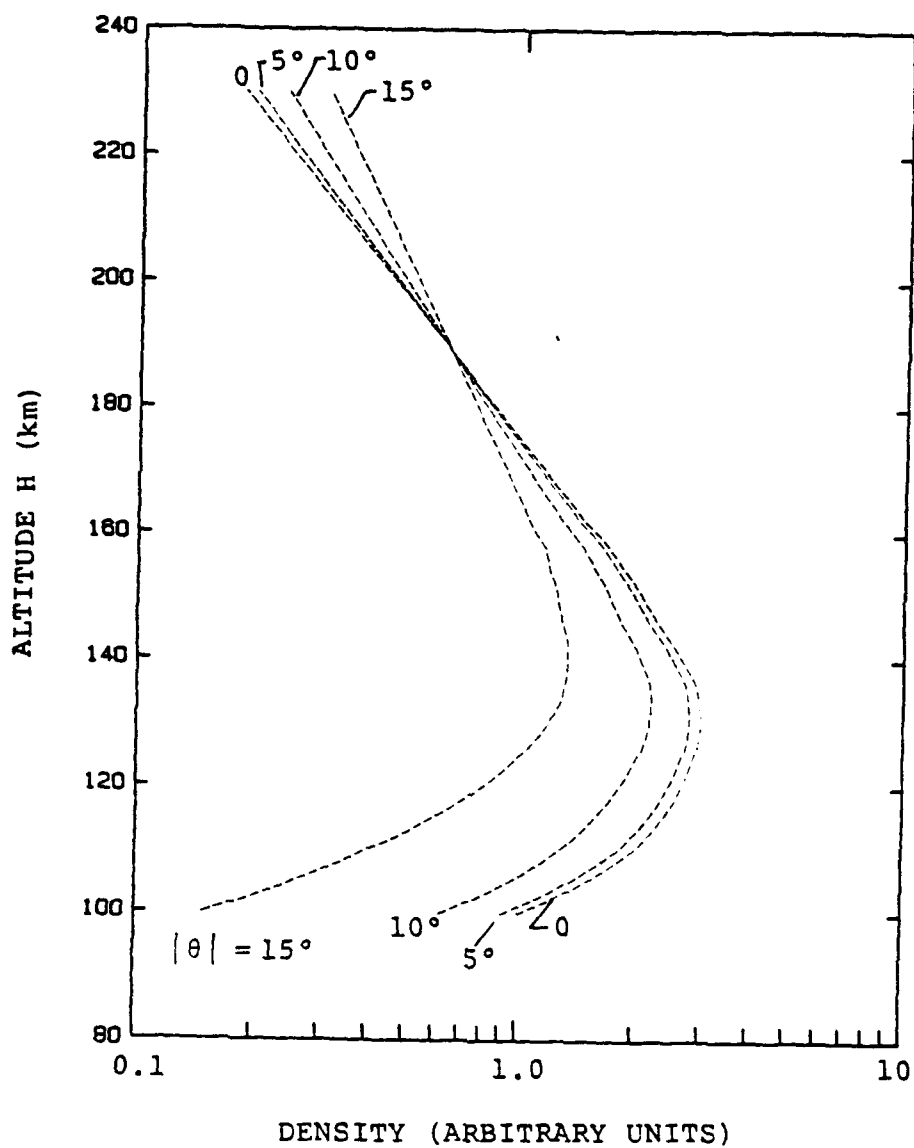


Fig. 5. Horizontal density variation for Case A. The model profiles $n(H,0)$ and $n(H,15^\circ)$ are shown as well as interpolated profiles for $\theta = 5^\circ$ and $\theta = 10^\circ$.

it by the Abel inversion routine described earlier. The recovered profile is the solid curve in Fig. 6; the dashed curve is the "true" density profile $n(H,0)$. The error is less than 10 percent.

3.2.2 Retrieval Error for Case B

For this case, the two reference profiles corresponding to $\theta = 0$ and 15 degrees were interchanged. Now $n(H,\theta)$ vs. θ for H less than 190 km is a minimum rather than a maximum at $\theta = 0$. Figure 7 shows the reference profiles and the interpolates for 5 and 10 degrees. The recovered profile and $n(H,0)$ are compared in Fig. 8. The retrieval error is within 10 percent above 120 km.

3.2.3 Retrieval error for Case C

For this case (Fig. 9) the model profile for $\theta = 15$ degrees is the same as for Case B; for $\theta = 0$ the density profile is one-third the 15-degree profile. Note that the density variation from $\theta = 0$ to 10 degrees is 100 percent for all altitudes. Figure 10 shows that the retrieval error above the density peak is less than 20 percent, but reaches 100 percent at the lowest altitude.

3.2.4 Summary

For the reasons stated in Section 3.2 one would expect horizontal density variations to produce rather small errors in the vertical profiles recovered by limb inversion. We modelled three different cases representing maximum horizontal variations between roughly 50 and 100 percent. These could represent just the even parts of still larger actual density variations. If actual atmospheric density variations over 10 or 15 degrees of latitude or longitude have even parts that vary by less than 50 percent, then, indeed, the retrieval error is small, on the order of 10

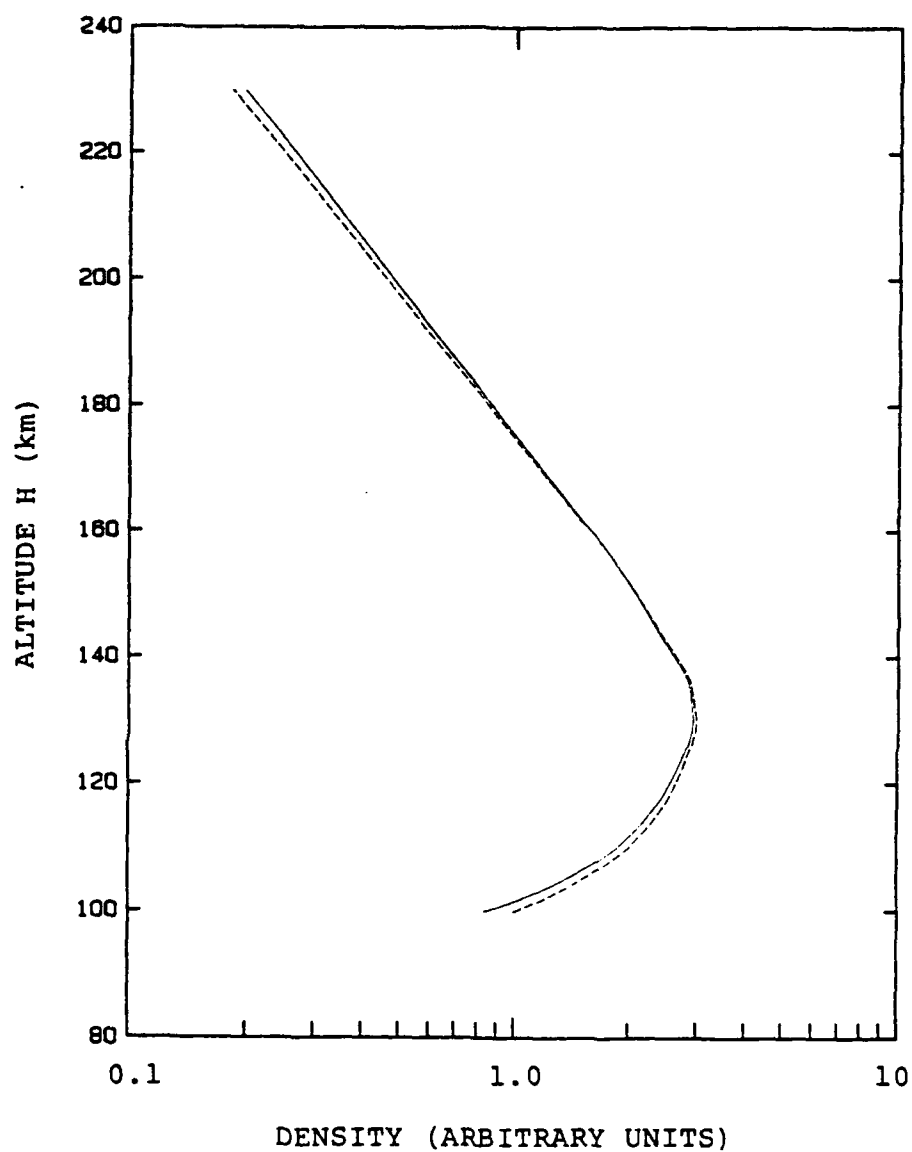


Fig. 6. Recovered density profile for Case A (solid curve) and the density profile $n(H,0)$. The magnitude of retrieval error is less than 10 percent at all altitudes.

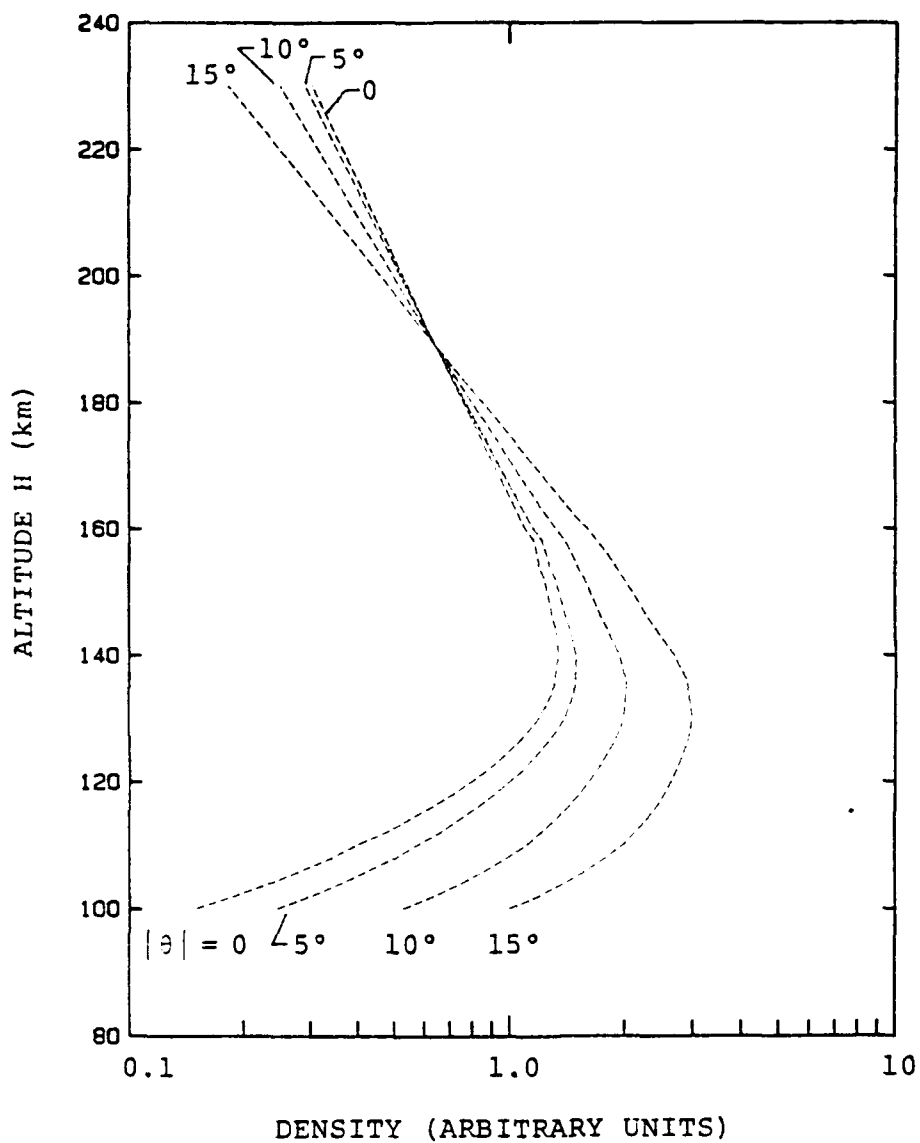


Fig. 7. Horizontal density variation for Case B: The models $n(H,0)$ and $n(H,15^\circ)$ of Case A have been interchanged. Below 190 km, the density is now a minimum at $\theta = 0$, rather than a maximum.

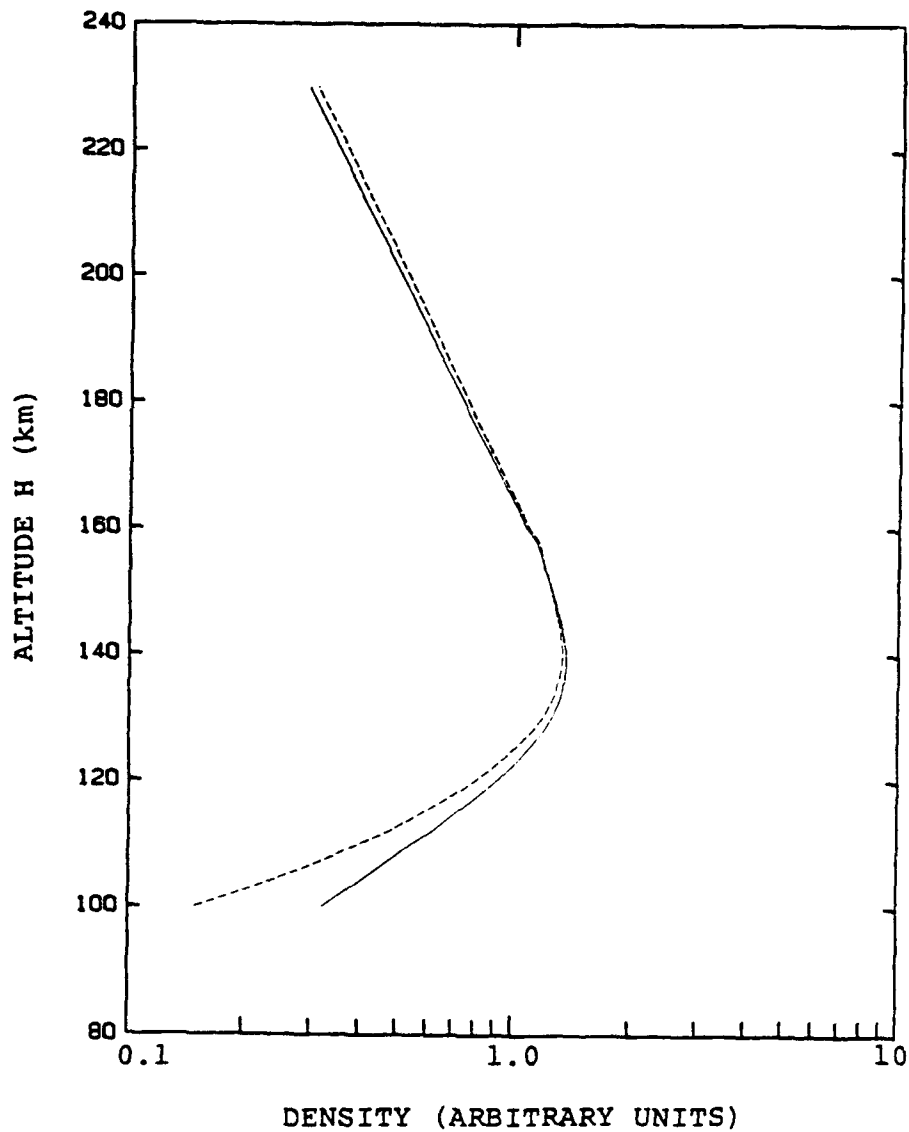


Fig. 8. Recovered density profile for Case B (solid curve) and the density profile $n(H,0)$. The magnitude of the retrieval error is less than 10 percent above 120 km.

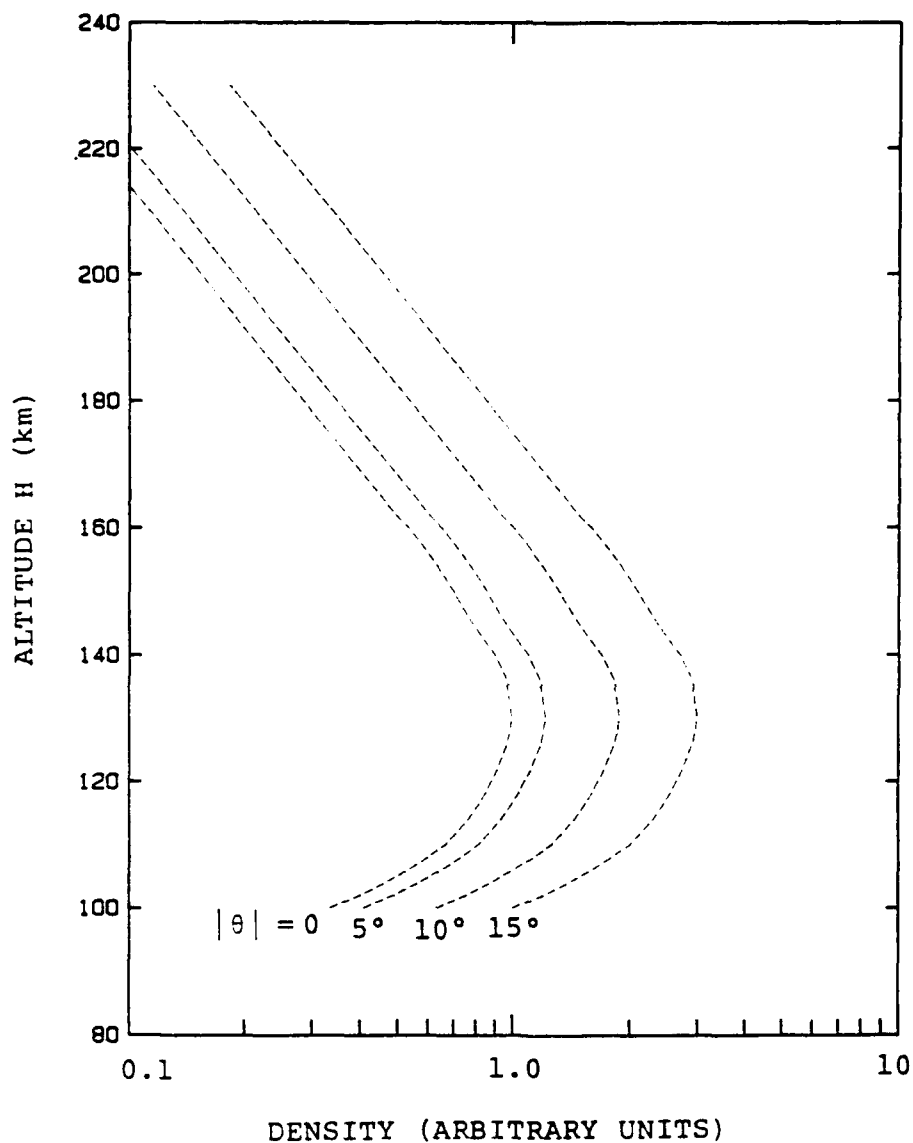


Fig. 9. Horizontal density variation for Case C: The model $n(H, 15^\circ)$ is the same as for Case B. The model $n(H, 0)$ is equal to $n(H, 15^\circ)/3$. Note that the density is a minimum at $\theta = 0$ for all altitudes.

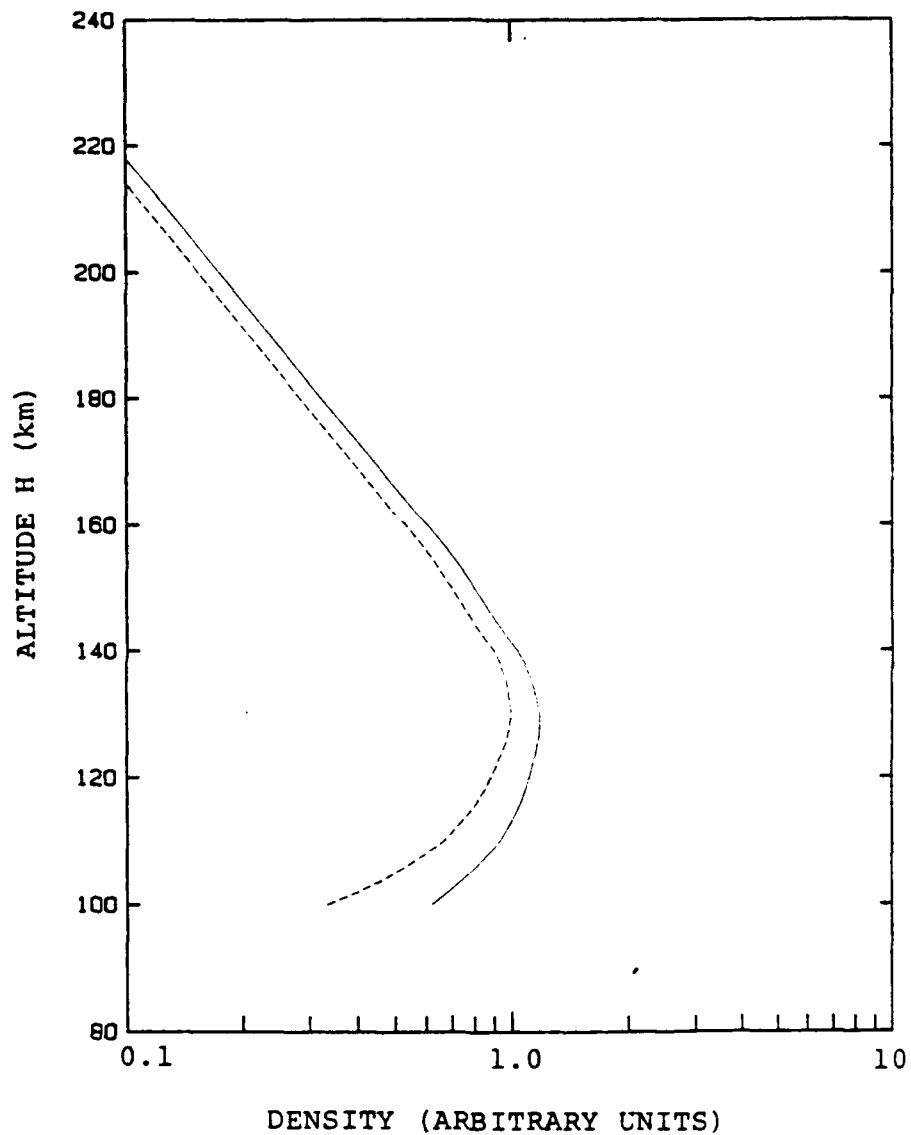


Fig. 10. Recovered density profile for Case C (solid curve) and the density profile $n(H,0)$. Despite a 100-percent variation in density over the limb path (0 to 10°), the retrieval error is less than ~ 20 percent above the altitude of the peak.

percent or less. An exception is the case of a layered species like excited NO; a significant retrieval error could occur for a 50-percent variation, but only at altitudes far below the altitude of the peak (Fig. 8).

Travelling ionospheric disturbances (TIDs) are known to be related to waves in the thermosphere, and appear to have horizontal wavelengths [Forbes, et al, 1987] that are predominantly "large scale" (from 1000 to 2000 km) and "medium scale" (100 to 300 km). As mentioned above, limb sounding of the atmosphere above 100 km can potentially be affected by density variations within 20 degrees (± 10 degrees) of latitude/longitude, which corresponds to a horizontal distance of about 2300 km. A wave with period much smaller than 2300 km, eg., a medium-scale TID, would have little effect on the limb retrieval results since the contributions of the peaks and troughs would average out in the measured limb radiance. On the other hand, only a fraction of one period of a disturbance whose wavelength is longer than 2300 km would effect the limb retrievals. Data and modelling results on tidal and gravity wave thermospheric perturbations are described by Killeen and Roble [1988]; densities measured between 160 and 220 km in a series of Air Force satellite accelerometer experiments has been analyzed by Forbes, et al [1987]. Results presented in these references indicate that a 50-percent variation in density over 2300 km is about the largest to be expected during geomagnetically quiet periods, and that 100-percent or larger variations can occur in a geomagnetically active period. We conclude that the corresponding maximum quiet-period retrieval error and a possible active-period retrieval error are roughly 10 and 20 percent, respectively.

SECTION 4

CYBER VERSION OF THE SHARC CODE

One of the first efforts of the present study was to transport the SHARC code from the Apollo computer to the Cyber 860 computer system at GL. We had planned to use SHARC so extensively that it would not have been practical to perform the computations on the slower Apollo computer. After the code was successfully transported, the plan was revised; fewer SHARC executions were required, and these were performed on the Apollo computer (in fact, by GL rather than ARC).

The Cyber and Apollo systems have significant differences with respect to word length, available direct-access memory, the operating system and the Fortran 5 instruction set, intrinsic function names, and file naming restrictions. These differences made it necessary to modify the SHARC Fortran coding and to develop execution procedures unique to the Cyber/NOS operating system. The modified code was executed successfully for one of the test cases described in the SHARC documentation, which served to validate the modifications.

A complete set of files allowing compilation and execution of SHARC on the Cyber/NOS system is contained in a tape that resides presently in the Computing Center tape library at GL. These files are described in Appendix B.

SECTION 5

PERFORMANCE PREDICTIONS FOR THE SPIRIT 3 RADIOMETER BANDS

The objective of the work reported in this section is to estimate the performance of the SPIRIT 3 radiometer in the earth limb mode. The effort consisted of first predicting the uncertainties in the atmospheric limb radiance profiles to be obtained by the SPIRIT 3 radiometer. These uncertainties, which are the predicted total system noise levels equated to radiance at the entrance aperture, and which we have computed as a function of tangent height for each of the five radiometer bands, represent estimates of the error bars on the earth limb backgrounds to be measured, and therefore are in themselves useful measures of performance. The second part of the effort consisted of determining corresponding uncertainties in vertical profiles of volume emission rate recovered from the limb radiance data. Both types of uncertainty are dependent on the actual limb radiance profile; our estimates are based on synthetic data computed for the SPIRIT 3 bands using the SHARC code.

5.1 Predicted Uncertainty in Measured Limb Radiance Profiles

The expected rms error in a measured limb radiance profile depends on

- a.) a model for the total system noise, including the contribution of photon noise, and the effects of coadding and gain setting (integration time),
- b.) a model for the actual limb radiance profile, and
- c.) a strategy that determines the gain switching for the detector array, and the position (tangent height range) of the radiometer FOV in successive horizontal scans.

The model for total system noise was developed as a simple set of equations, given below. Telephone conversations with Clair Wyatt of Space Dynamics Laboratory and material presented

by him at the CDR meeting for SPIRIT 3 are the basis for the equations.

The detector output, in electrons per sample, is

$$DOUT = RAD \cdot (TAU \cdot LAM) \cdot (A \cdot OMEGA) / (hc) \cdot Q \cdot T_{int} \quad (1)$$

where RAD is the band radiance at the aperture, TAU is the band transmittance, LAM is the band center wavelength (hc/LAM is the energy of a photon of wavelength LAM), $A \cdot OMEGA$ is the sensor throughput (aperture area times solid-angle IFOV), $Q = 0.9$ is the detector quantum efficiency, and T_{int} is the integration time. For a given SPIRIT 3 band (given TAU , LAM), the above equation gives

$$DOUT = RAD \cdot (TAU \cdot LAM) \cdot T_{int} \cdot 3.625 \times 10^{13} \quad (1a)$$

if RAD is in W/cm^2 sr, wavelength LAM is in microns, and T_{int} is in seconds.

The corresponding radiometer band output in counts is

$$COUNTS = DOUT / 209 \quad (2)$$

where 209 is the root-sum-square of 91, 49, 73, 14 and 166:

91 = the A/D noise

49 = the analog electronics noise

73 = the mux noise

14 = the photon noise at the level corresponding
to $COUNTS = 1$

166 = the shot noise for $T_{int} = 13.9 \times 10^{-3}$ sec

The last four are noise values before coadding; the A/D noise is not affected by coadding.

The noise level, in electrons per sample, after coadding, is

$$DNOIS = [91^2 + (49^2 + 73^2 + 14^2 \cdot COUNTS + 166^2 \cdot T_{int}/13.9 \times 10^{-3}) / (DUTCYC \cdot 13.9 \times 10^{-3} / T_{int})]^{1/2} \quad (3)$$

where the coadding duty cycle $DUTCYC$ is 0.25 for the shortest integration time ($T_{int} = 0.217$ ms), and is 1.0 for all other integration times. Note that $DNOIS = 209$ for $COUNTS = 1$ and $T_{int} = 13.9 \times 10^{-3}$ sec., i.e., $DNOIS = 209 = DOUT$ from Eq. (2).

The signal-to-noise is $SNR = DOUT/DNOIS$, and the system noise level in radiance units (the uncertainty in the measured limb radiance) is RAD/SNR :

$$\text{Uncertainty in } RAD = RAD \cdot DNOIS / DOUT = RAD / SNR \quad (4)$$

Table 1 gives the values of LAM and TAU for the five radiometer bands. Using the values for band E and the above equations, we calculated the noise levels shown in Table 2 for the four different integration times. The table shows values of RAD (second column), $COUNTS$ (fourth column), $DOUT$ (fifth column), $DNOIS$ (sixth column), the uncertainty in RAD , the SNR and the integration time (7th through last columns). The first column gives the photon rate (quanta/sec) incident on the detector, which is equal to $DOUT / (Q \times T_{int})$. Note that each row in the table corresponds to an integral number of output bits NB (third column); the corresponding number of counts is 2^{NB-1} .

Given the "actual" limb radiance at a particular tangent height, i.e., the value of RAD in Eq. (1a), one can use the above equations to calculate a corresponding limb radiance uncertainty, provided the integration time is defined. Three different strategies were considered for switching the gain and for overlapping successive scans; these determine the integration time for each tangent height, as described below. The SHARC code

Table 1. SPIRIT-3 Radiometer Bands

Band	Center Wavelength LAM (μm)	Trans. TAU	BAND LIMITS* (μm)	
A	8.5	0.40	5.47	11.96
B	7.2	0.66	5.47	9.08
C	12.2	0.41	10.06	14.51
D	15.0	0.40	12.70	17.54
E	23.0	0.34	16.40	30.70

*used for SHARC radiance computations

Table 2. SPIRIT 3 EARTH LIMB MODE DYNAMIC PERFORMANCE FOR BAND E -- FROM EQS. (1-4)

-----INPUT-----		-----OUTPUT-----			-NOISE-	-----PERFORMANCE-----		
(q/s)	(W/cm2 sr)	(bits)	(Cnts)	(el/spl)	(el/spl)	NOISE (W/cm2 sr)	SNR	T _{int} (ms)
1.7E+04	5.3E-11	1	1	209	209	5.31E-11	1	13.900
5.0E+04	1.6E-10	2	3	627	210	5.33E-11	3	13.900
1.2E+05	3.7E-10	3	7	1463	212	5.38E-11	7	13.900
2.5E+05	8.0E-10	4	15	3135	216	5.47E-11	15	13.900
5.2E+05	1.6E-09	5	31	6479	223	5.65E-11	29	13.900
1.1E+06	3.3E-09	6	63	13167	236	6.00E-11	56	13.900
2.1E+06	6.7E-09	7	127	26543	262	6.64E-11	101	13.900
4.3E+06	1.4E-08	8	255	53295	306	7.76E-11	174	13.900
8.5E+06	2.7E-08	9	511	106799	379	9.62E-11	282	13.900
1.7E+07	5.4E-08	10	1023	213807	494	1.25E-10	433	13.900
3.4E+07	1.1E-07	11	2047	427823	667	1.69E-10	641	13.900
1.7E+07	5.4E-08	8	255	53295	156	1.59E-10	341	3.475
3.4E+07	1.1E-07	9	511	106799	192	1.95E-10	555	3.475
6.8E+07	2.2E-07	10	1023	213807	249	2.53E-10	858	3.475
1.4E+08	4.3E-07	11	2047	427823	335	3.40E-10	1277	3.475
6.8E+07	2.2E-07	8	255	53295	110	4.45E-10	487	.869
1.4E+08	4.3E-07	9	511	106799	123	4.99E-10	868	.869
2.7E+08	8.7E-07	10	1023	213807	146	5.94E-10	1461	.869
5.5E+08	1.7E-06	11	2047	427823	184	7.48E-10	2322	.869
2.7E+08	8.7E-07	8	255	53295	109	1.77E-09	488	.217
5.5E+08	1.7E-06	9	511	106799	123	1.99E-09	871	.217
1.1E+09	3.5E-06	10	1023	213807	146	2.37E-09	1464	.217
2.2E+09	6.9E-06	11	2047	427823	184	2.99E-09	2325	.217
4.4E+09	1.4E-05	12	4095	855855	243	3.94E-09	3525	.217

was used to obtain limb radiance profiles for each of the SPIRIT-3 radiometer bands.*

The three strategies are summarized in Table 3. The first, labeled "Case 0", assumes the gain can be set independently for each detector in the vertical array. While this case is not realistic for SPIRIT 3, it leads to an upper bound on the performance of a single detector for all possible strategies. The integration times are determined differently for increasing than for decreasing signals (but in accordance with the current SPIRIT 3 design). Increasing signal is assumed here to correspond to successively lower IFOV tangent heights, with the integration time initially set at the maximum value, 13.9 ms, for the largest tangent height. The limb radiance profile is examined at successively lower tangent heights, and the corresponding band output, in counts, is calculated. When the number of counts has become greater than 2^{11} , the integration time is divided by four; this new integration time is used to determine the counts (and also the uncertainty in limb radiance) until the number of counts again exceeds 2^{11} . Up to three such gain changes are allowed. The case of decreasing signal corresponds to examination of the limb radiance profile from low to high tangent altitudes; the lowest is 60 km, with the integration time set initially at the minimum value, 0.217 ms. The integration time is increased by a factor of four each time the number of counts falls below 2^8 . Again, up to three gain changes are allowed. If $COUNTS > 2^{12}$ for any detector element after these tests on the increasing or decreasing signal, the element is saturated (regardless of which strategy is used).

*We did not use the Cyber version of SHARC described in Section 4 to compute these profiles, but rather used limb radiances that had already been obtained by Dr. Harold Gardiner of AFGL using the Apollo version of the code.

Table 3. Gain Switching Cases

CASE 0: SWITCH GAIN (CHANGE T_{int}) INDEPENDENTLY FOR EACH DETECTOR

Increasing signal: $T_{int} \rightarrow T_{int}/4$ if $COUNTS > 2^{11}$

Decreasing signal: $T_{int} \rightarrow 4T_{int}$ if $COUNTS \leq 2^8$

Change T_{int} up to three times

CASE 1: SWITCH GAIN FOR ALL 192 ELEMENTS

Increasing signal: $T_{int} \rightarrow T_{int}/4$ if $COUNTS > 2^{11}$
for more than 14 elements

Decreasing signal: $T_{int} \rightarrow 4T_{int}$ if $COUNTS \leq 2^8$
for more than 14 elements
(14 elements ≈ 4 km)

FOV footprints are 60-115 km, 115-170, ... (no scan overlap)

CASE 2: SAME AS CASE 1, EXCEPT

Use only lower 25 km of 55-km array,

Displace bottom of FOV by 25 km in successive (overlapped) scans

(effective FOVs are 60-85 km, 85-110, ...)

The Case-1 strategy is more representative of those planned for SPIRIT 3. The essential difference from Case 0 is that the gain is switched for all 192 elements comprising the vertical FOV column. Also, the gain is switched only if 15 or more elements meet the criteria on the number of counts. Thus, for a limb downscan (increasing signal), the integration time is divided by four if it is found that N elements, where $N > 14$, have outputs greater than 2^{11} counts. Each of the N elements can be located anywhere in the 192-element array.

The 192-element FOV column corresponds to a vertical footprint (range of tangent heights) of roughly 55 km; 14 contiguous elements span approximately four km. The limb radiance uncertainties computed for the Case 1 strategy will, of course, depend on where the FOV is located within the earth's limb. We assumed, for Case 1, that a complete limb scan is executed as a sequence of non-overlapping horizontal sweeps of the 192-element FOV. As indicated in Table 3, the successive IFOV footprints are 60-115 km, 115-170 km, ..., ; they would occur in this order for a limb upscan (decreasing signal), and in the reverse order for a limb downscan.

In some of the SPIRIT 3 bands, the predicted limb radiance at 60 km tangent height is very large compared to the limb radiance at 115 km. In this situation, the Case 1 strategy may result in relatively poor performance (much lower SNR) at 115 km; ie., the short integration time needed to avoid $COUNTS > 2^{11}$ near 60 km must also be used at 115 km. This is obviously the result of the large FOV and the non-overlapped scan pattern rather than the gain-switching criteria.

The third strategy (Case 2) is the same as for Case 1 except that successive horizontal scans correspond to a

vertical displacement of 25 km in the tangent height of the bottom edge of the FOV. It is assumed in our computation that data measured by the elements in the overlapped portion of the FOV, ie., the upper 30 km of the FOV, is discarded; in practice, it might be coadded to corresponding data obtained in a prior/subsequent horizontal scan, if it happened that the gain level was the same for both scans. The effective FOVs for Case 2 are 60-85 km, 85-110 km,

Following is a presentation of results for the uncertainty in measured limb radiance. These will include only bands D, E and A, only the NIGHT case (AFGL supplied SHARC radiance profiles for both DAY and NIGHT), but will include all three gain switching/scan overlap strategies.* The nine figures show both the SHARC limb radiances and the computed uncertainties for the different strategies. The limb radiances correspond to a Summer model atmosphere for 60-degrees latitude, a 1000K exospheric temperature, and include earthshine effects.

Figure 11 shows the results for Band D, Case 0. The dashed line is the SHARC limb radiance profile and the full line(s) show the corresponding limb radiance uncertainty, ie., the system noise in radiance units. Gain-switching occurs at different tangent heights for the limb upscan than for the limb downscan, resulting in the three "hysteresis loops" in the uncertainty profile. Upward and downward arrows differentiate between the sides of the loops corresponding to the upscan (decreasing signal) and downscan (increasing signal) cases, respectively. The figure shows that the SNR is greater than 500 below 120 km tangent height, and is greater than 10 up to approximately 180 km.

*Results for bands B and C and for the DAY case can be easily produced by ARC codes that implement the described procedures. These codes could be generalized to model other strategies for gain switching/scan overlap.

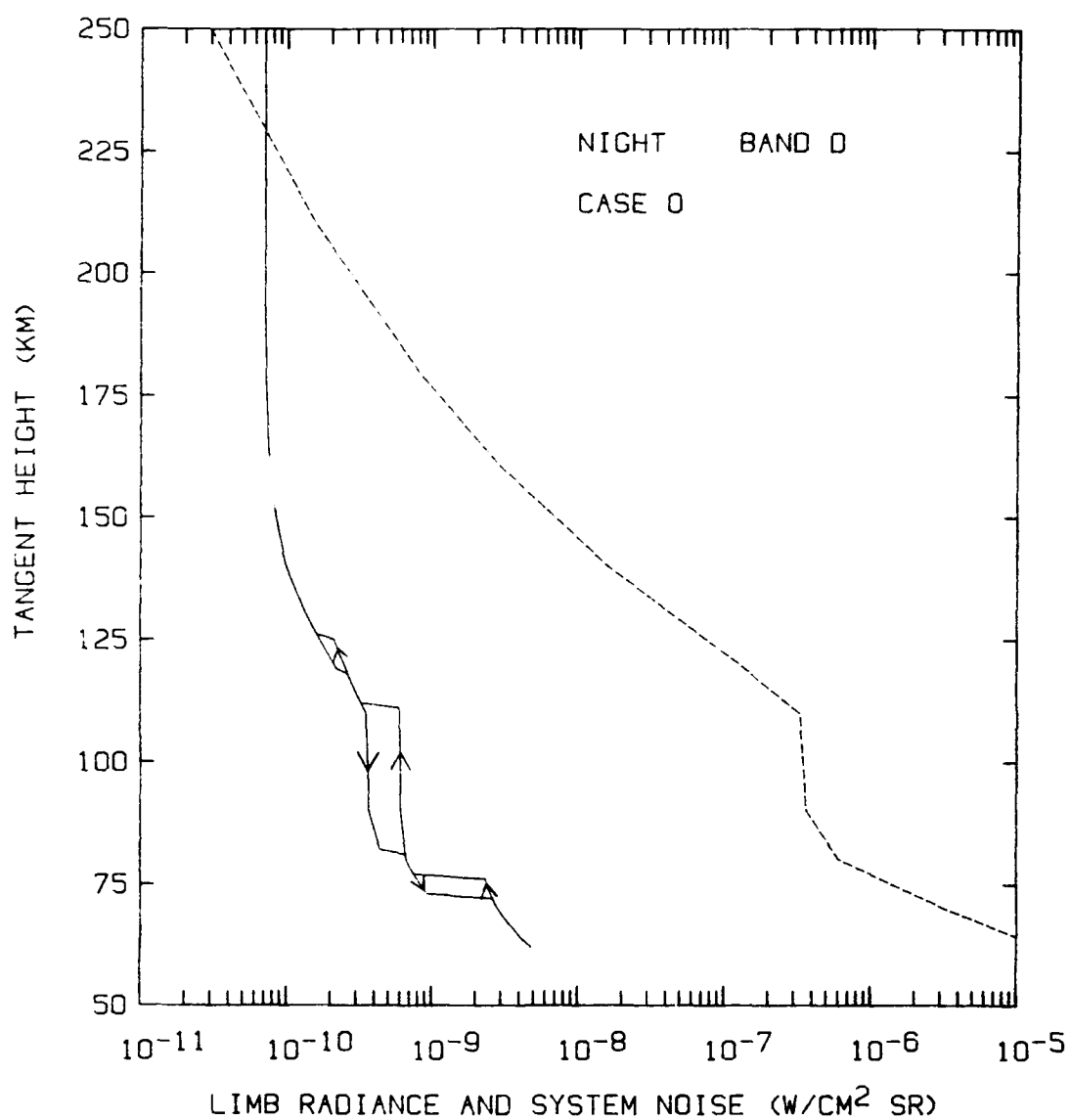


Figure 11. Limb radiance profile (dashed curve) and expected rms uncertainty in the measured limb radiance (full lines), for Band D, Case 0.

The full lines in Fig. 11 begin at 60 km and are continuous over the entire range of tangent heights, indicating that none of the data is saturated. The uncertainty in radiance is infinite when saturation occurs and hence it cannot be plotted. In the following figures any gaps in the full lines indicate saturation. Similarly, if one of the full lines begins at a tangent height greater than 60 km, then the data is saturated from 60 km to this tangent height.

Figure 12 shows the results for Band D, Case 1. Numbers in parentheses next to any large step in the radiance uncertainty, or at the bottom end of the uncertainty curve, are the number of gain changes that resulted in this step. The other numbers, not in parentheses, are the corresponding tangent height. Thus, Fig. 12 shows that for the first segment of the upscan, when the FOV covered 60-115 km, an initial gain change was required (because $COUNTS \leq 2^8$ for 15 or more elements). After this four-fold increase in the integration time, the output from elements below 69 km were saturated. When the FOV was moved upward to 115-170 km tangent height, two additional (simultaneous) gain changes were required. Similarly, in the last segment of the downscan, when the FOV was moved to 60-115 km, three simultaneous gain changes (reductions in integration time) were required to avoid $COUNTS > 2^{11}$ for 15 or more elements. Saturation occurs only between 60 and 62 km. In spite of the large step in the downscan uncertainty at 115 km, the SNR below this tangent height is greater than approximately 150; for the Case 0 strategy, $SNR \geq 500$ below 150 km tangent height.

Figure 13 shows the results for Band D, Case 2. As expected, the hysteresis loops are much smaller than for Case 1. In fact, the SNR for most tangent heights is approximately the same as for the unrealistic Case 0

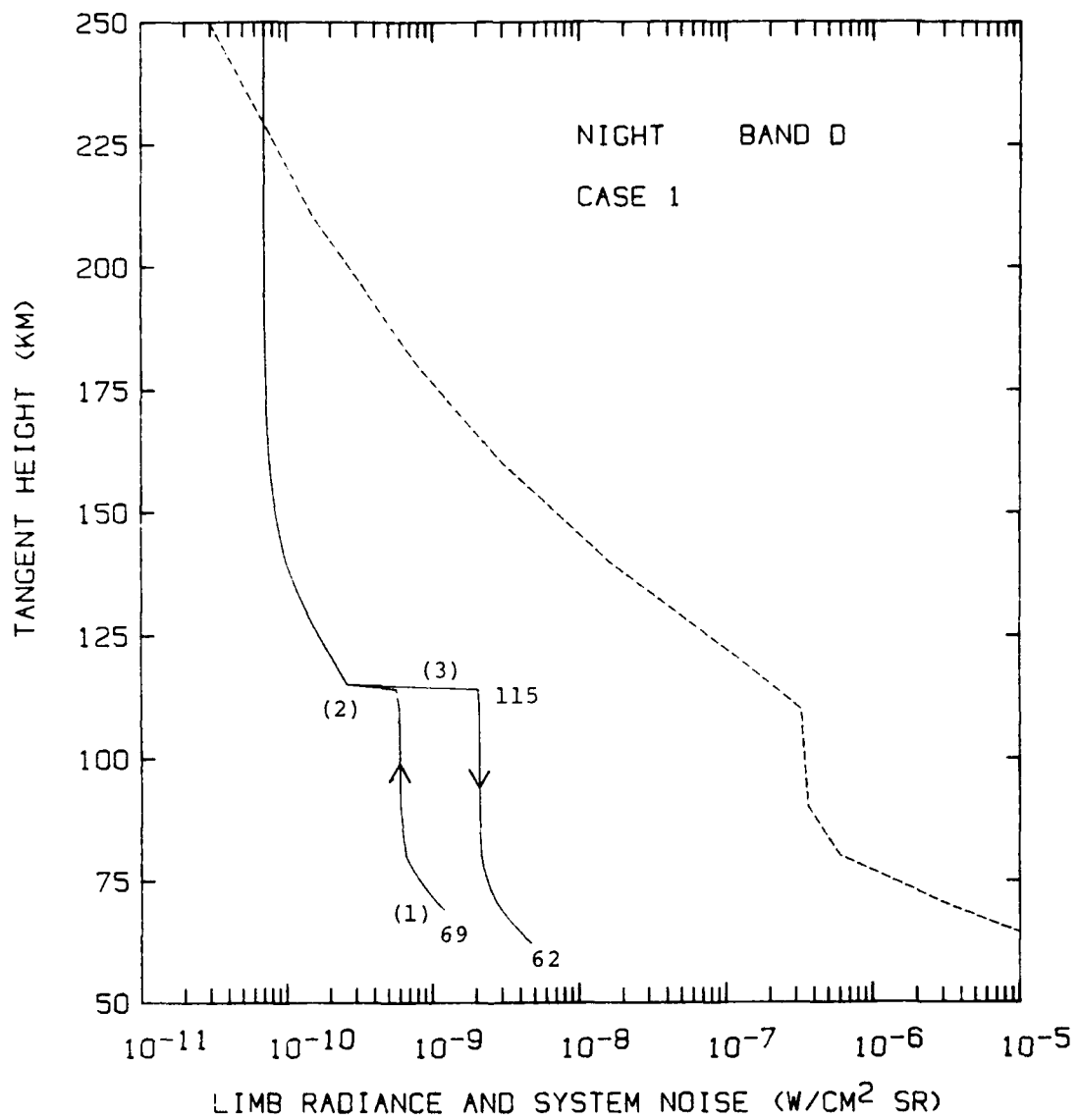


Figure 12. Same as Fig. 11, except the results represent Case 1.

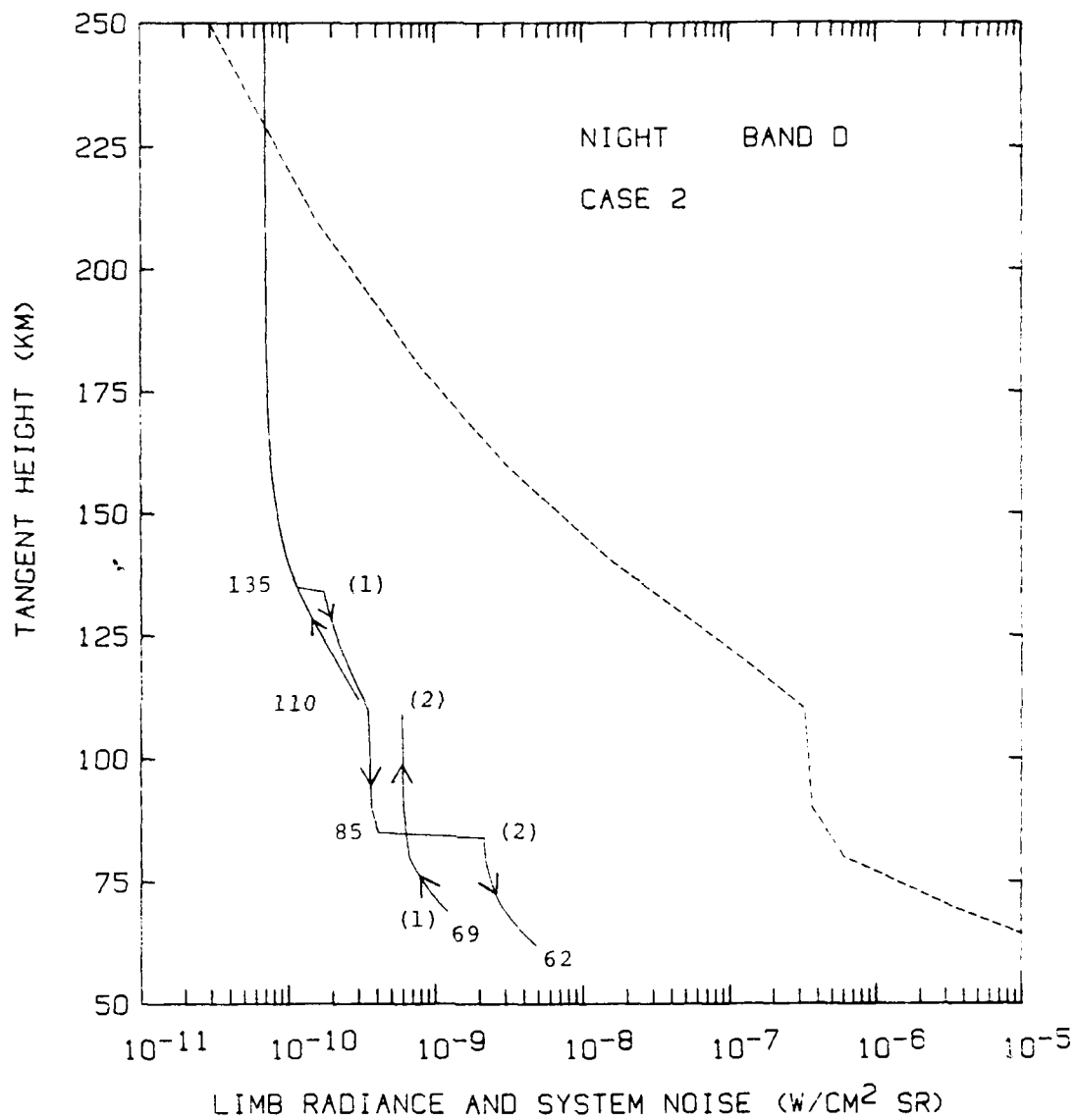


Figure 13. Same as Fig. 11, except the results represent Case 2.

strategy (compare Figs. 11 and 13). There is, however, a narrow range of tangent heights near 110 km where the data is saturated.

Figures 14, 15 and 16 show the results for Band E, Cases 0, 1 and 2, respectively. Note that the SNR is quite low, approximately 3.5, between 100 and 115 km for Case 1. The Case 2 strategy improves the SNR to approximately 15 or 20 over this range of tangent heights. The results for Band A, Cases 0, 1 and 2 are shown in Figs. 17, 18 and 19, respectively. Again, the Case 2 strategy results in a considerable improvement in SNR over the Case 1 strategy below 115 km tangent height.

5.2 Predicted Uncertainty in Retrieved Volume Emission Rate Profiles

The SHARC limb radiance profiles were inverted, both with and without the predicted SPIRIT 3 noise contribution, to obtain vertical profiles of volume emission rate and an estimate of the rms relative errors in these retrieved emission rates. The SPIRIT 3 noise contributions are based on the limb radiance uncertainty profiles described above.

The inversions were performed using the new derivative-free Abel inversion routine described in Section 2 and Appendix A. The Abel transform is valid only when the limb viewing path is optically thin, a condition which is not met for some of the bands, e.g., Band D, at the lower tangent heights. However, there generally will be some altitude (which we have not defined in the present study) above which the recovered volume emission rate profile is valid.

The following description of how the uncertainty in retrieved volume emission rate was computed will refer frequently to Fig. 20, which shows this error for Band D, Case 1. We first obtained the "true" volume emission rate

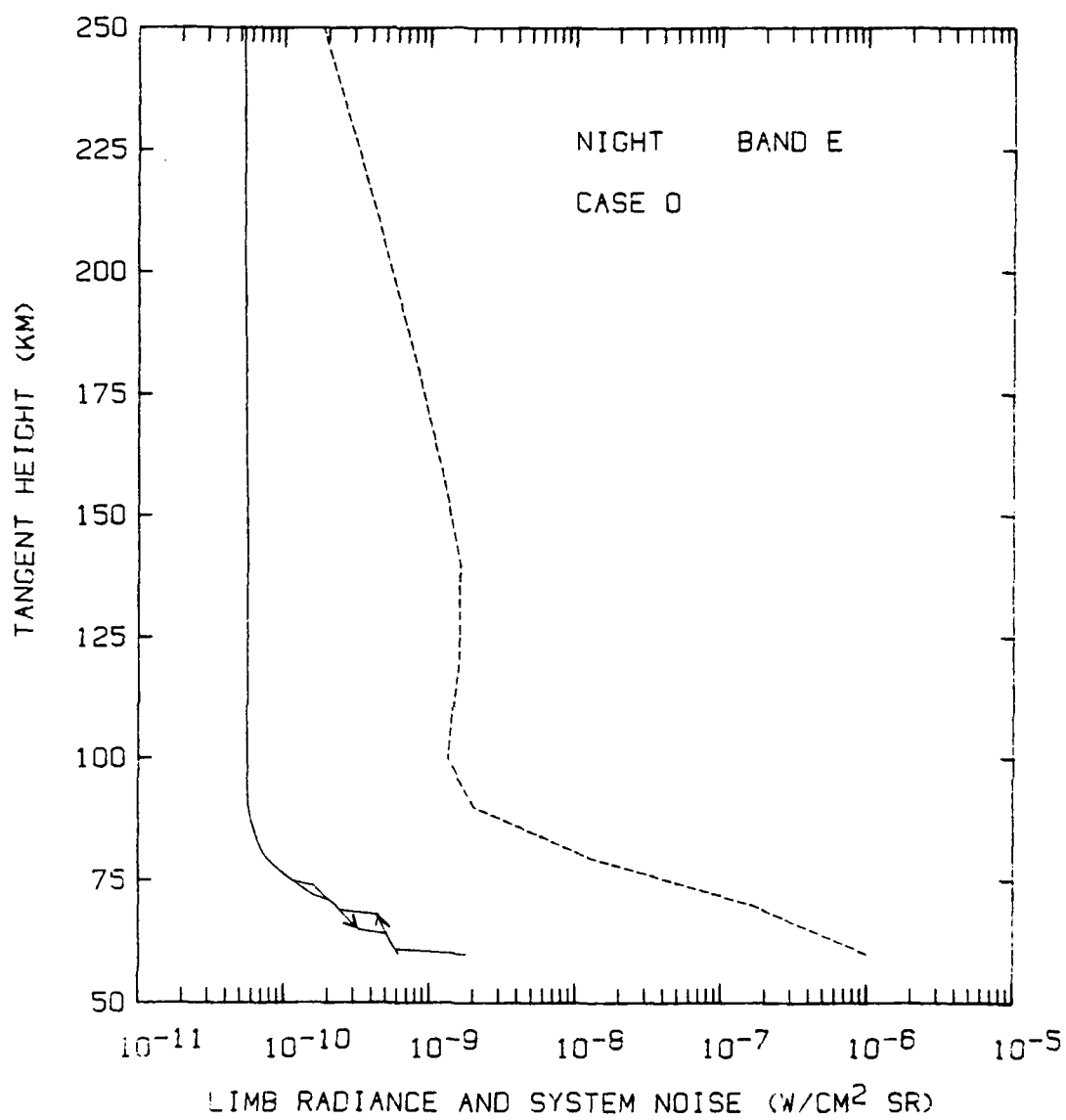


Figure 14. Same as Fig. 11, except the results represent Band E, Case 0.

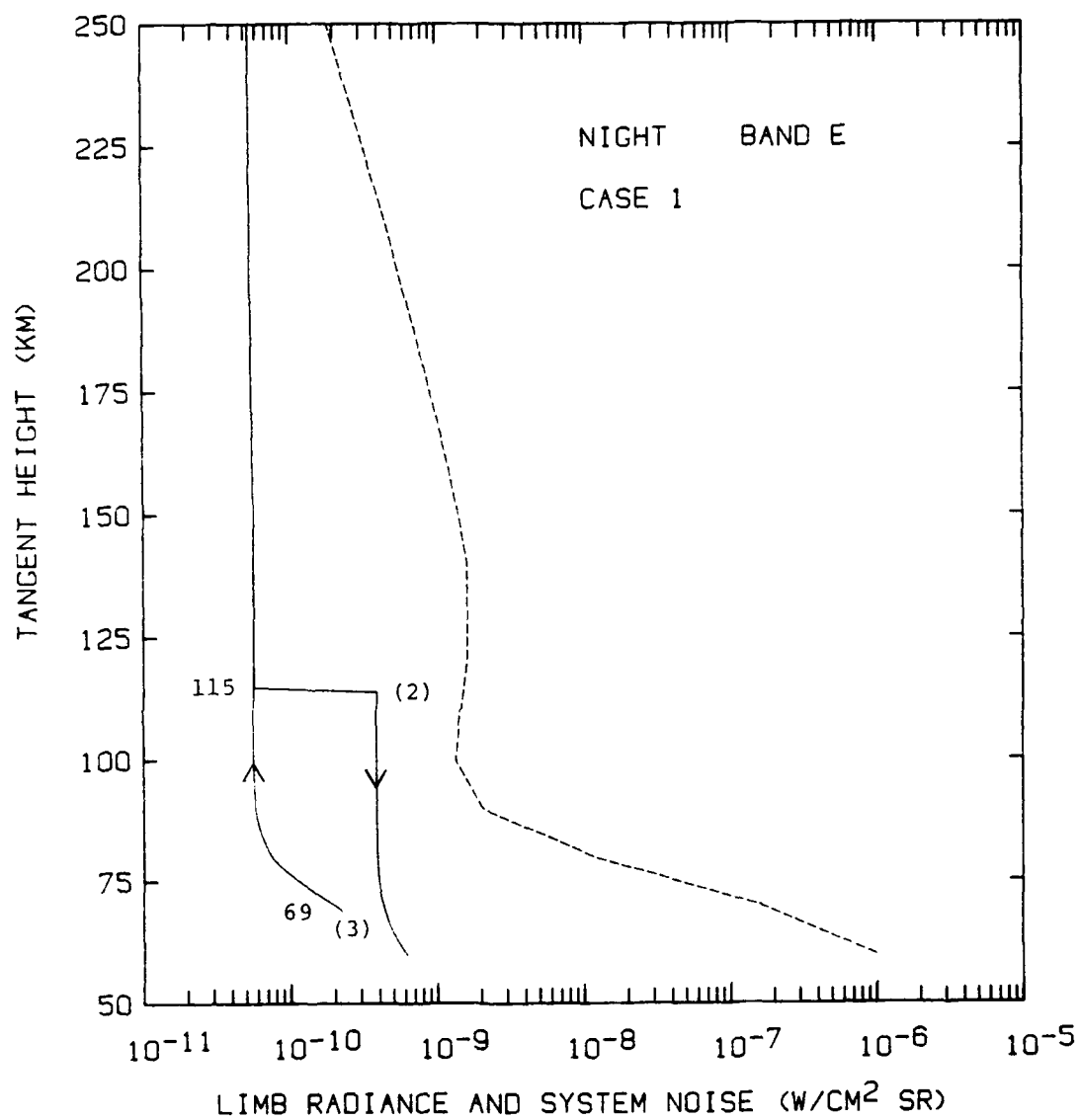


Figure 15. Same as Fig. 11, except the results represent Band E, Case 1.

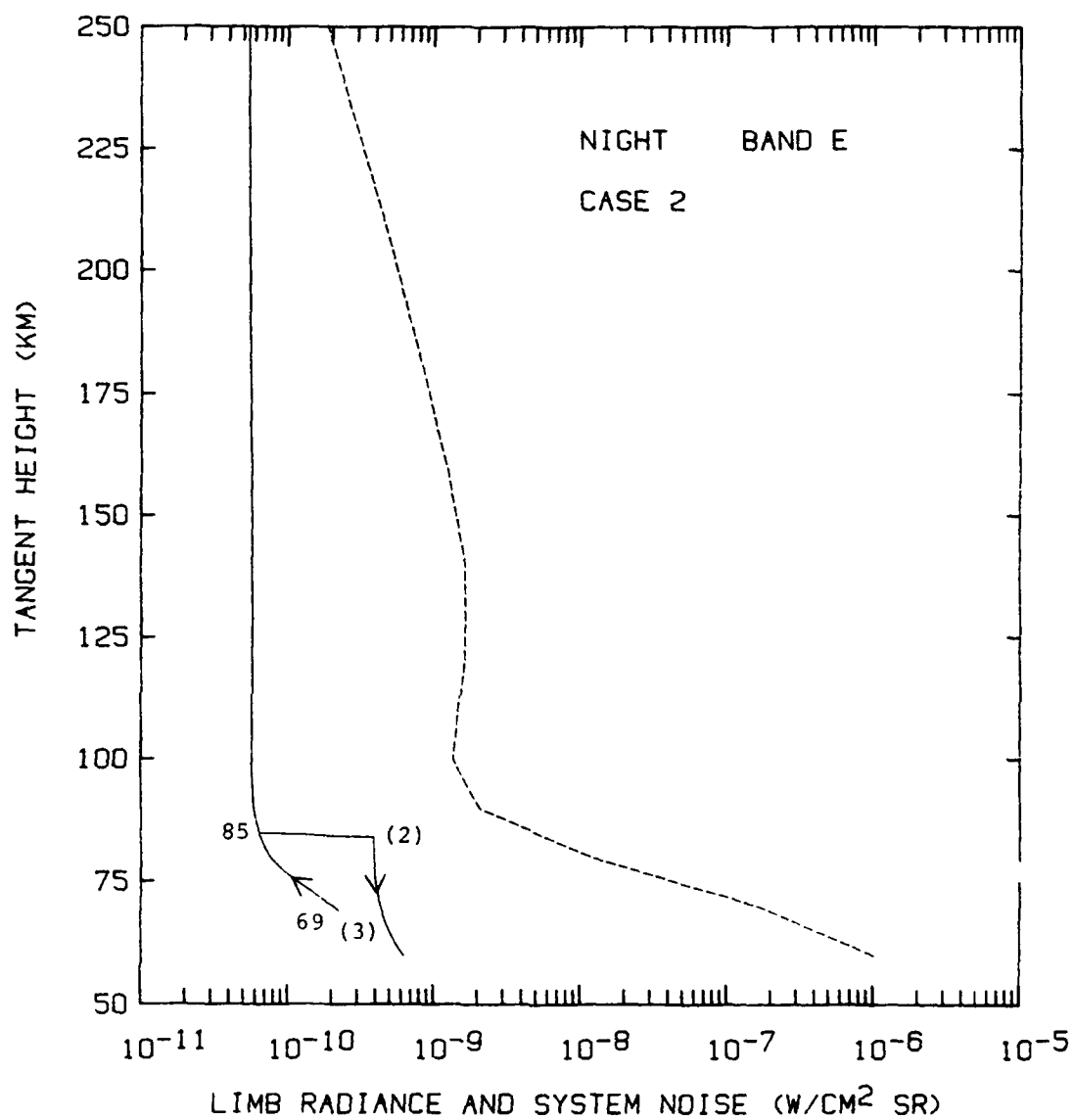


Figure 16. Same as Fig. 11, except the results represent Band E, Case 2.

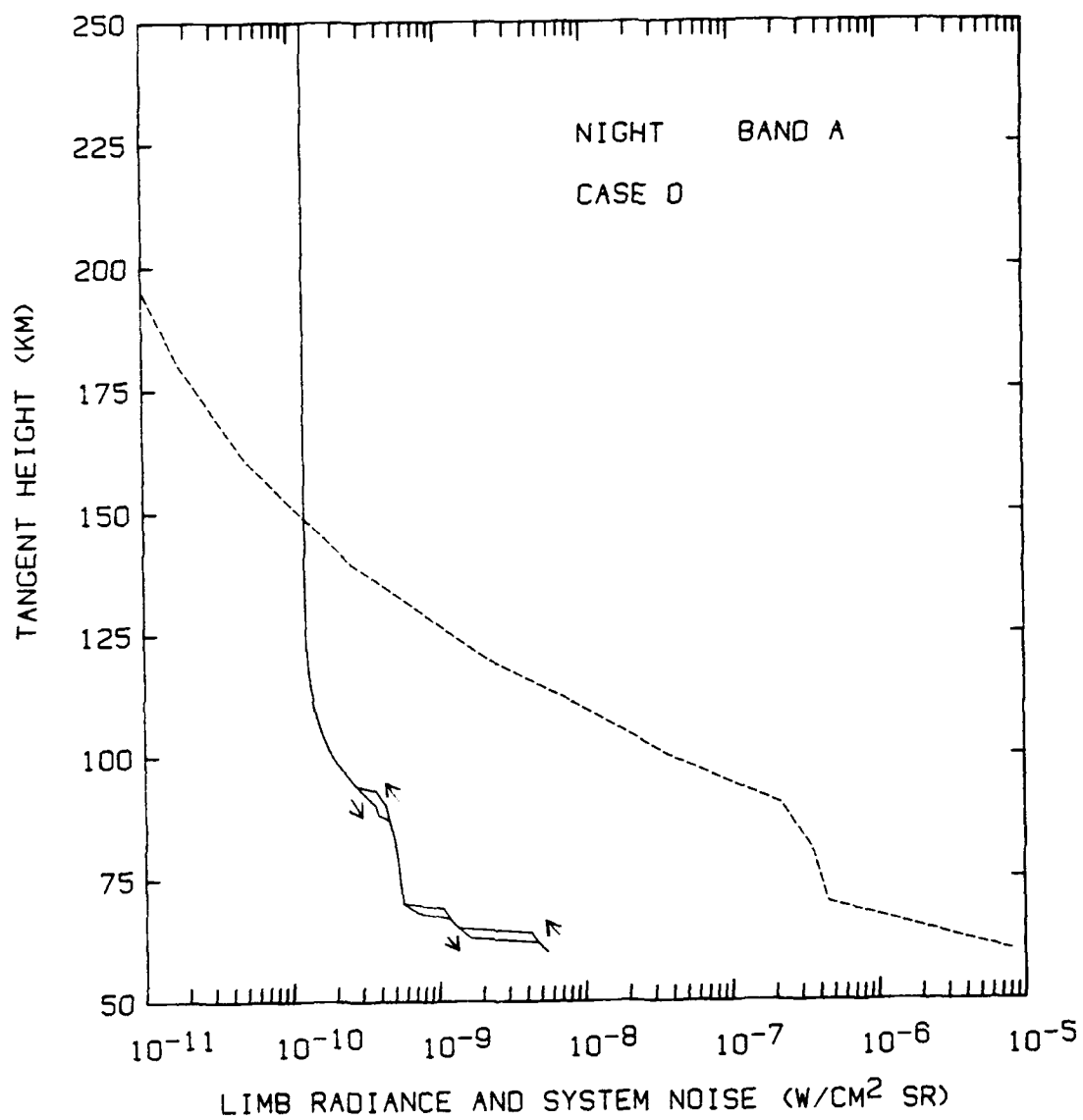


Figure 17. Same as Fig. 11, except the results represent Band A, Case 0.

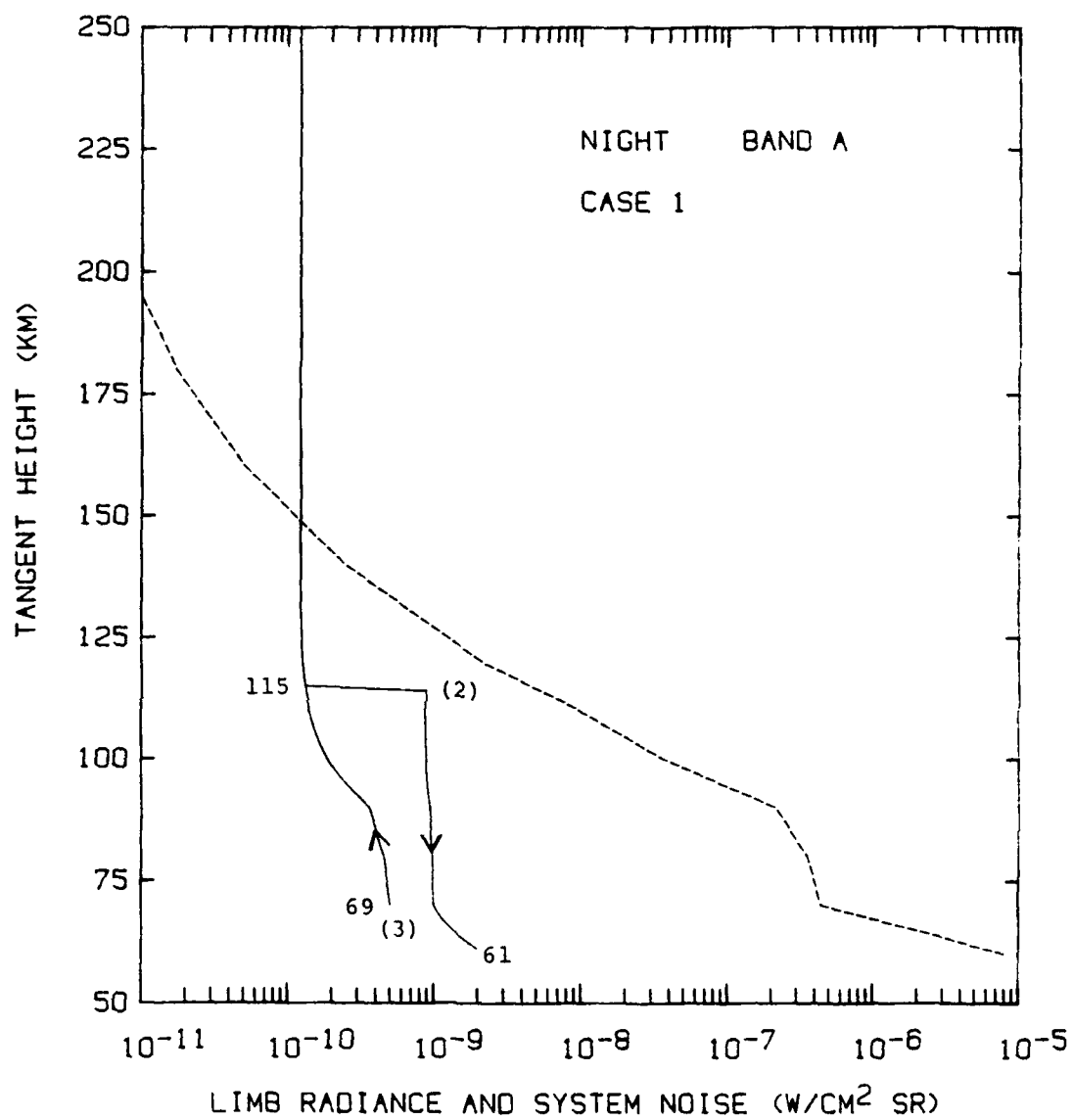


Figure 18. Same as Fig. 11, except the results represent Band A, Case 1.

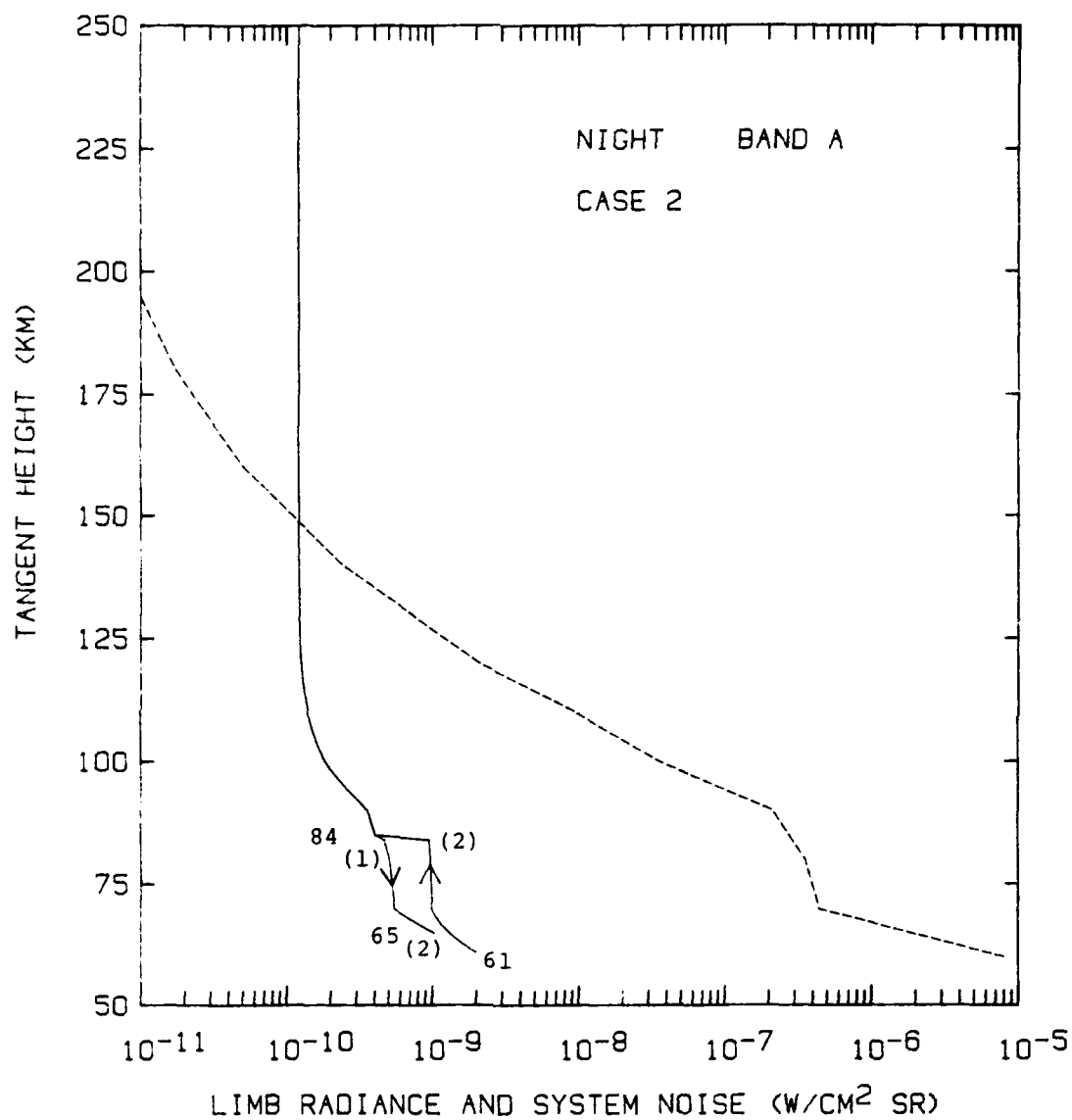


Figure 19. Same as Fig. 11, except the results represent Band A, Case 2.

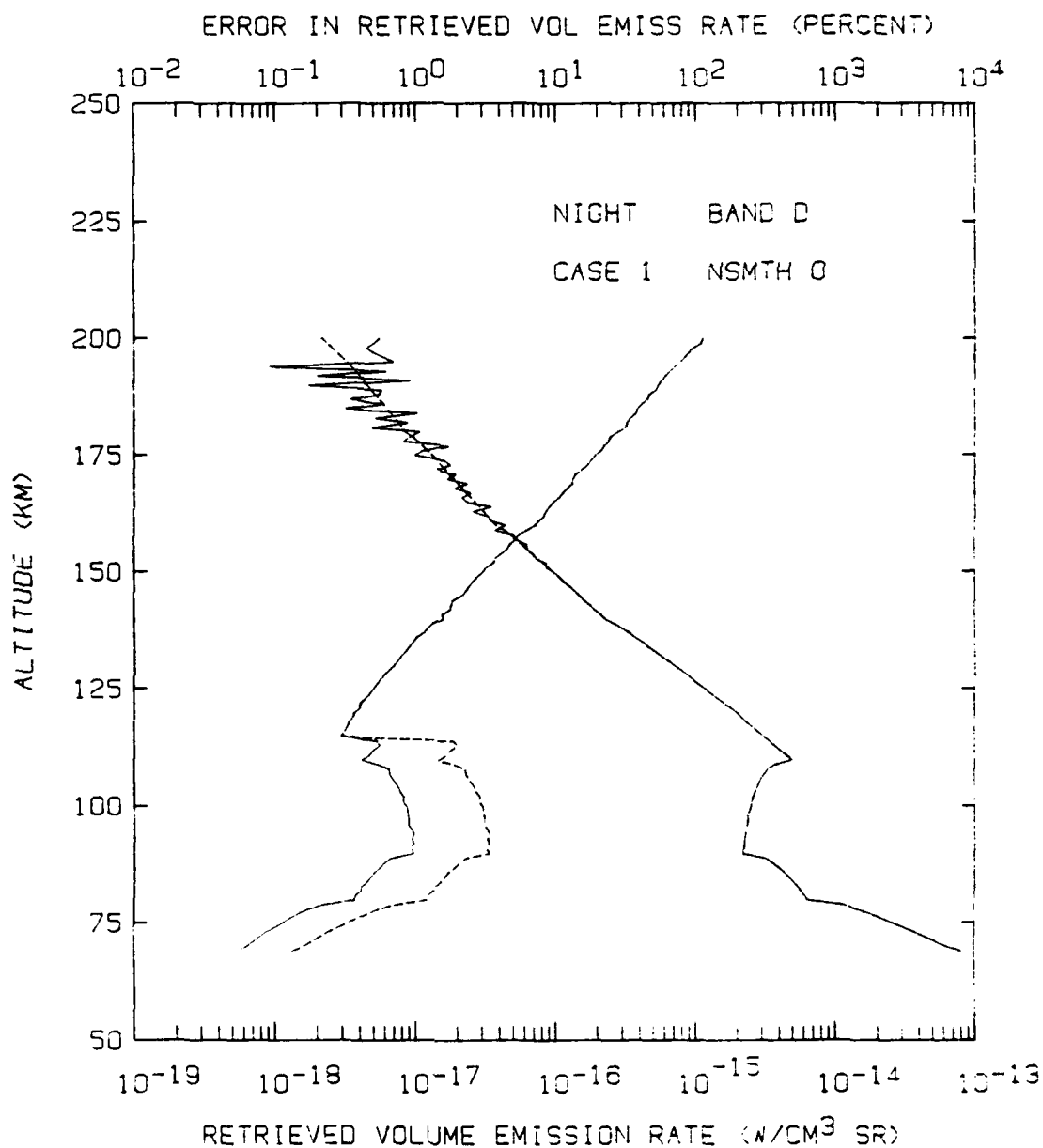


Figure 20. The "true" vertical profile of volume emission (dashed line), a typical retrieved profile (full line) and the predicted rms error in the retrieved profile (full and dashed lines); for Band D, Case 1 and no smoothing.

profile by applying the inversion routine to the noise-free SHARC limb radiance profile. For Band D, this emission rate profile is shown in Fig. 20 by the dashed line which tends to slope downward from left to right. Below 150 km it is indistinguishable from the full line representing a typical solution when noise is added to the SHARC limb radiance profile. The noise consists of a set of Gaussian pseudo-random numbers with rms level, at a given tangent height, equal to the predicted uncertainty in limb radiance (for Band D, Case 1, this is the full curve for the limb upscan in Fig. 11) multiplied by a factor accounting for the vertical resolution of the retrieval. In other words, the noise value at a particular tangent height is obtained by picking a random number from a unit normal population and then scaling it with respect to the predicted SPIRIT 3 noise level and by the resolution factor. The resolution factor is $3.5^{1/2}$, based on the assumption that the desired vertical resolution is one km (3.5 IFOVs subtend approximately one km at the tangent height).^{*} The $3.5^{1/2}$ reduction in noise level can be achieved by coadding.

After adding noise to the SHARC limb radiance profile at all tangent heights, we invert the profile to obtain the volume emission rate versus altitude at one km increments. The computer code written to perform these operations allows for optional smoothing of the noisy limb radiance profile before it is inverted. The process is repeated 1000 times, and then the rms relative error of the 1000-member ensemble of solutions is computed. The result is a prediction of the uncertainty in volume emission rate vs. altitude when this emission rate profile is obtained by derivative-free Abel inversion of SPIRIT 3 data. By basing the prediction on 1000 trials we are assured of a reasonably high confidence level (small statistical error) in our prediction. The

^{*}The limb radiance profiles and SPIRIT 3 noise levels were modelled to a resolution of one km in tangent height.

"typical" solution shown in Fig. 20 is the outcome of a single trial, and is representative of results to be expected using SPIRIT 3 data for Band D. This solution was obtained without smoothing of the noisy limb radiance profile. The smoothing procedure is described below.

The two curves in Fig. 20 that slope upward to the right above 125 km show the computed emission rate uncertainty for Band D, with the Case 1 gain switching/scan overlap strategy; values of uncertainty are given, in percent, on the upper scale. The full line corresponds to a limb upscan (decreasing signal), and the dashed line to a limb downscan. The uncertainty is less than one percent below 165 km.

The figures showing the uncertainty in retrieved volume emission rate have, like Fig. 20, a legend in the upper right-hand corner consisting of four parameters. The first identifies the SHARC limb radiance profile as a NIGHT or DAY case; we used only the NIGHT profiles supplied by GL. The second parameter is the SPIRIT 3 band; we considered only bands D, E and A. The third identifies the gain switching/scan overlap strategy -- Case 0, 1 or 2. The final parameter, NSMTH, is the number of times the noisy limb radiance profile has been smoothed; we performed computations only for NSMTH = 0 and NSMTH = 1. The smoothing consists of fitting a cubic equation to each 11 points of the profile (each 11 km of tangent height) and evaluating the cubic at the central (sixth) point. A set of weighting coefficients that effects this type of smoothing is given by Savitzky and Golay [1964]. A single smoothing pass will effectively reduce the noise level by roughly a factor of three while degrading the vertical resolution in the retrieved volume emission rate from one km to approximately three km.

Figure 21 shows results for the same combination of parameters as Fig. 20, except that NSMTH is 1 rather than 0.

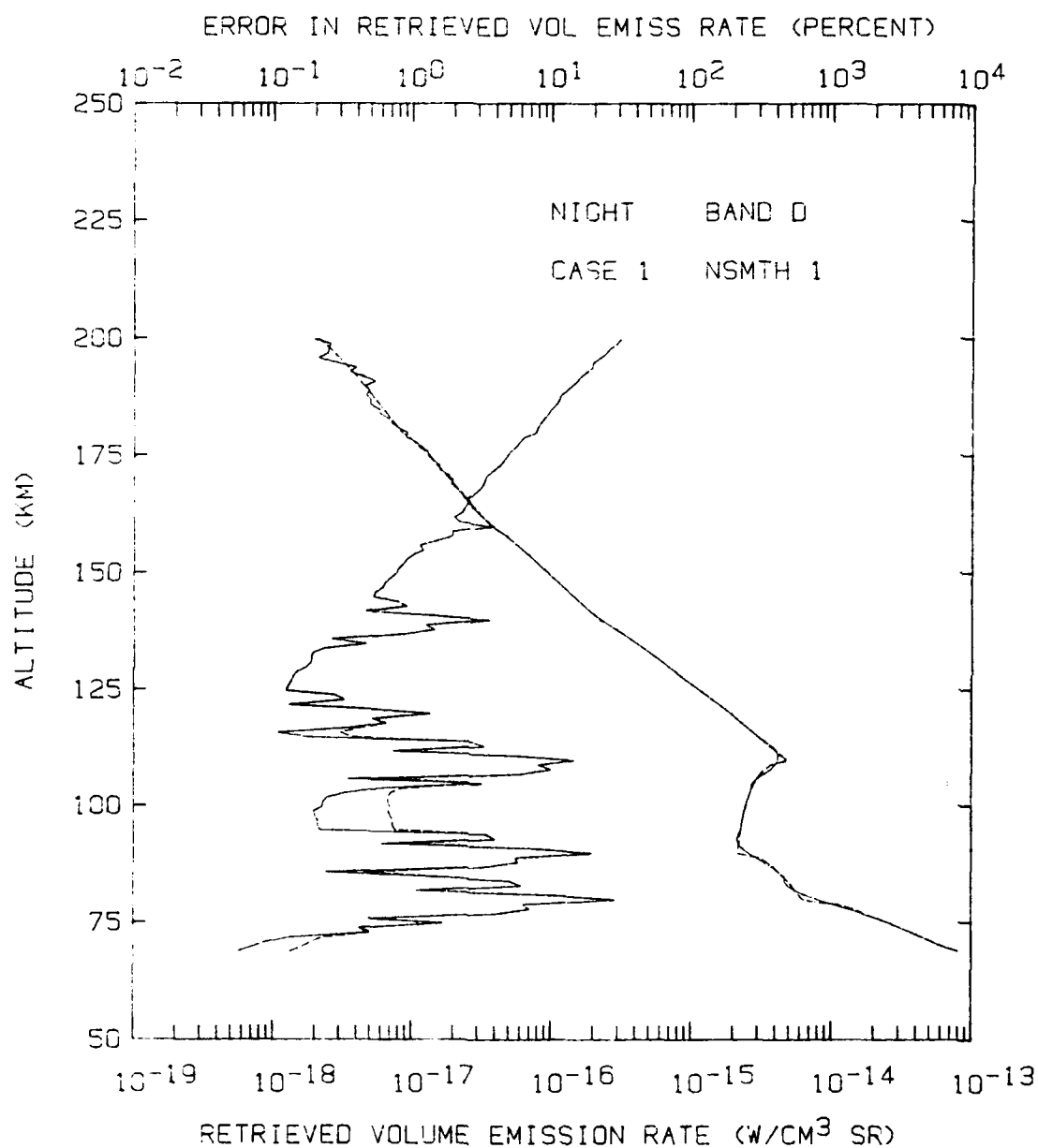


Figure 21. Same as Fig. 20, except the noisy limb radiance profile was smoothed once before the inversion.

The volume emission rate retrieved from the smoothed data (the typical solution shown in Fig. 21) is obviously a more reasonable solution, above 150 km, than the one obtained with no smoothing. Note that smoothing increases rather than decreases the error where there are sharp features in the true emission rate profile, eg., at 110 km.* Clearly, smoothing is not necessary for Band D below 125 km where the available SNR is very high.

Figure 22 shows the results obtained for Band D using the Case 2 strategy and no smoothing. The error in retrieved volume emission rate is less than approximately one percent at all altitudes lower than 135 km. It may be recalled that the limb radiance data for the limb upscan for this Band/Case was saturated over a narrow range near 110 km tangent height (see Fig. 13). We reconstructed the missing data by simple interpolation, which effectively reproduced the smooth SHARC radiance profile in this region.

Figures 23 through 25 show results for Band E. The error in retrieved volume emission rate is reduced significantly by smoothing or by using the Case 2 rather than Case 1 strategy, but even then the error above 100 km will be 10 to 100 percent, owing to low radiance levels.

Figures 26 and 27 show that the Band A volume emission rate can be accurately recovered below approximately 115 km, especially if the Case 2 strategy is used.

*If the retrieved profile is presented as a solution representing the degraded (3 km) resolution, then it would be reasonable to exclude from the error estimate the systematic component due to smoothing of real structure.

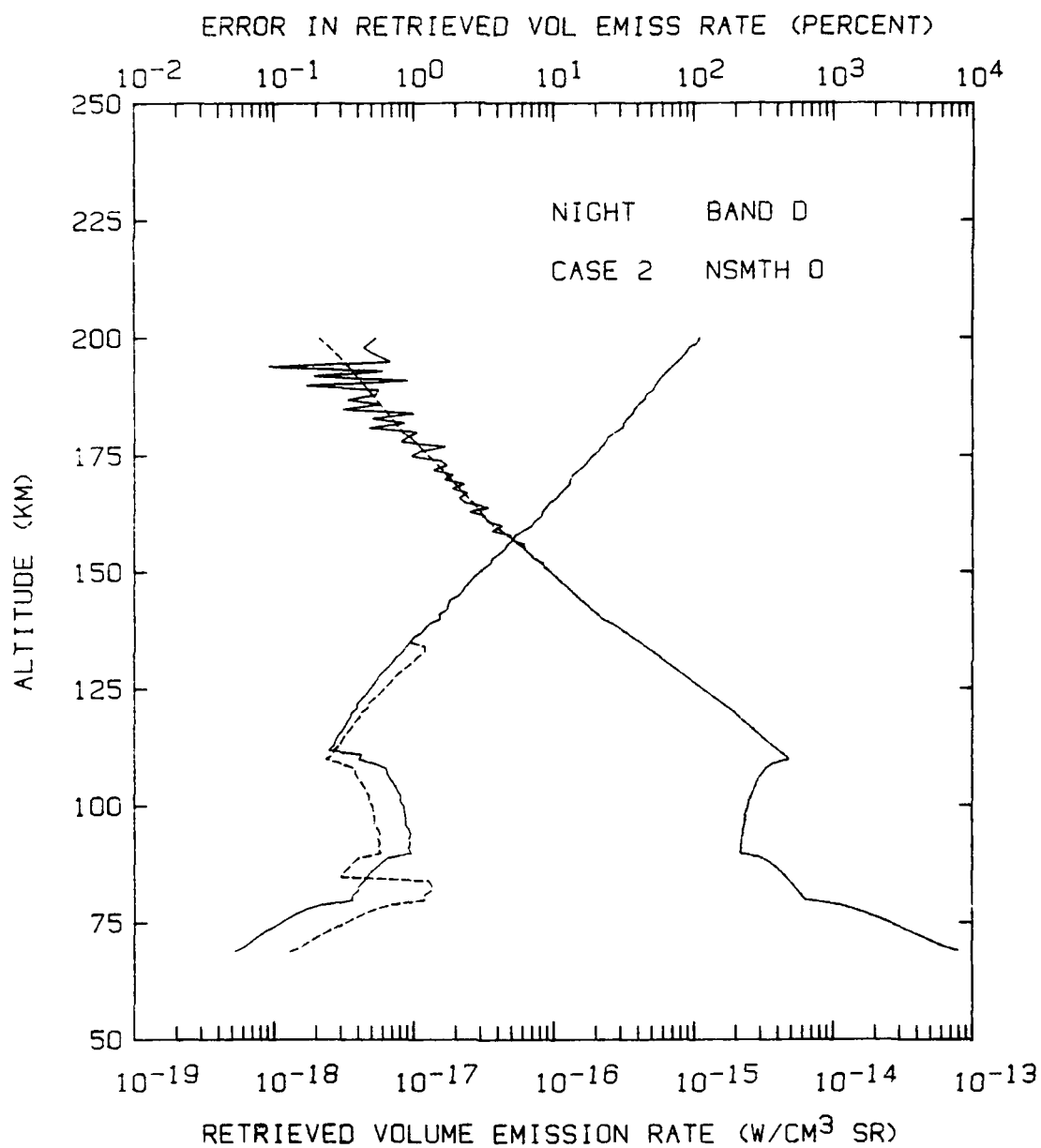


Figure 22. Same as Fig. 20, except the results represent Case 2.

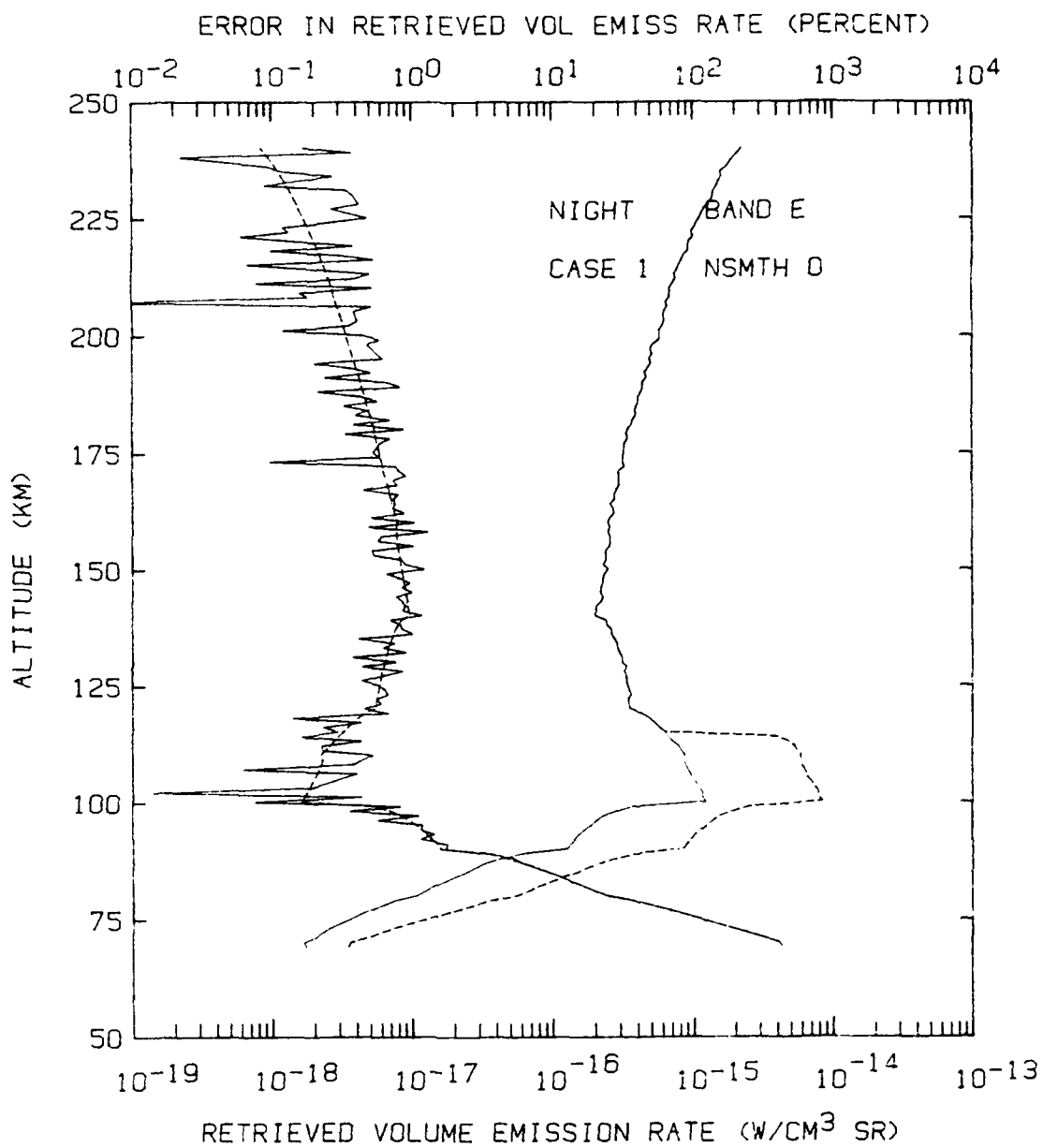


Figure 23. Same as Fig. 20, except the results represent Band E, Case 2.

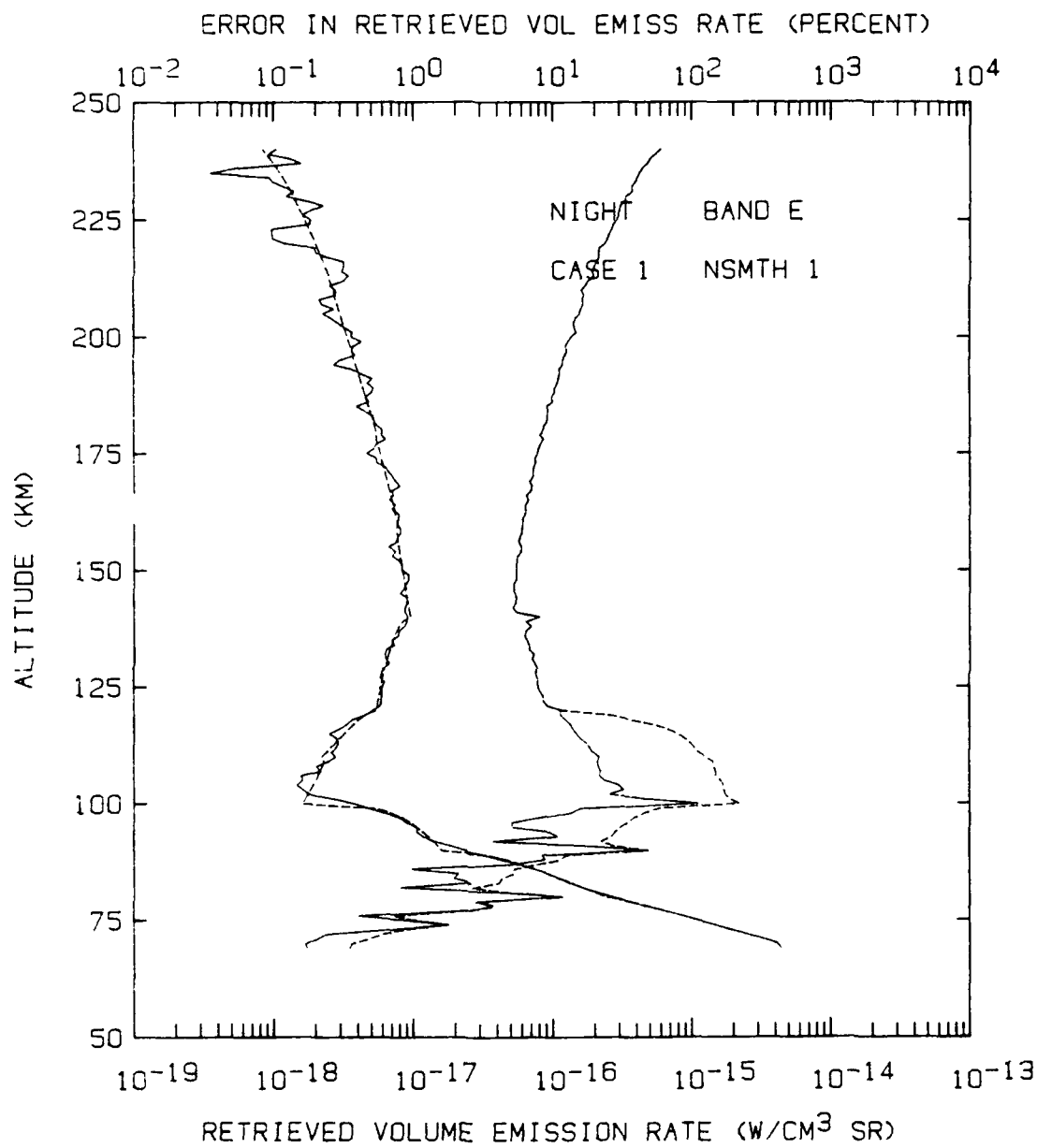


Figure 24. Same as Fig. 23, except $NSMTH = 1$.

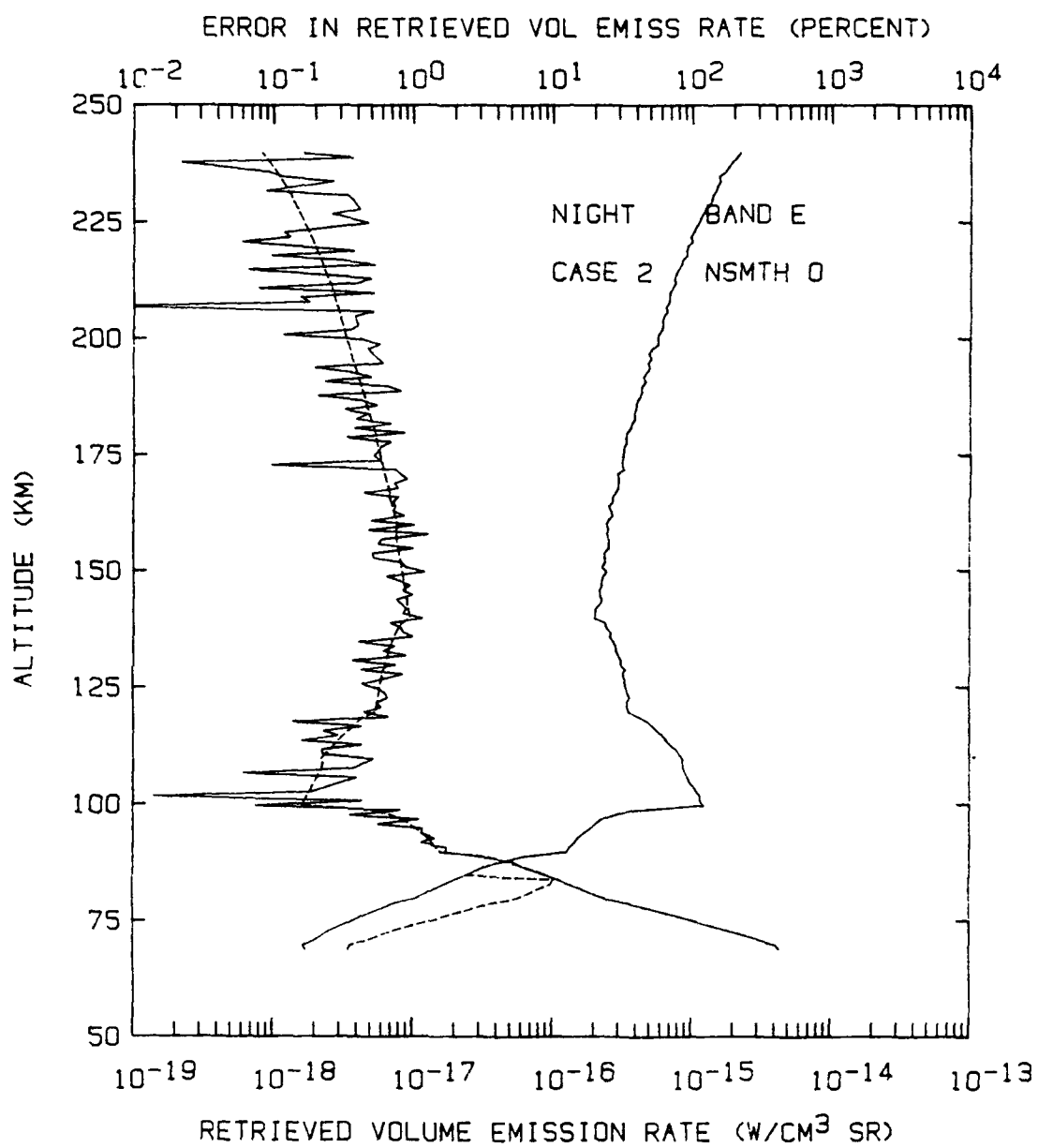


Figure 25. Same as Fig. 20, except the results represent Band E, Case 2.

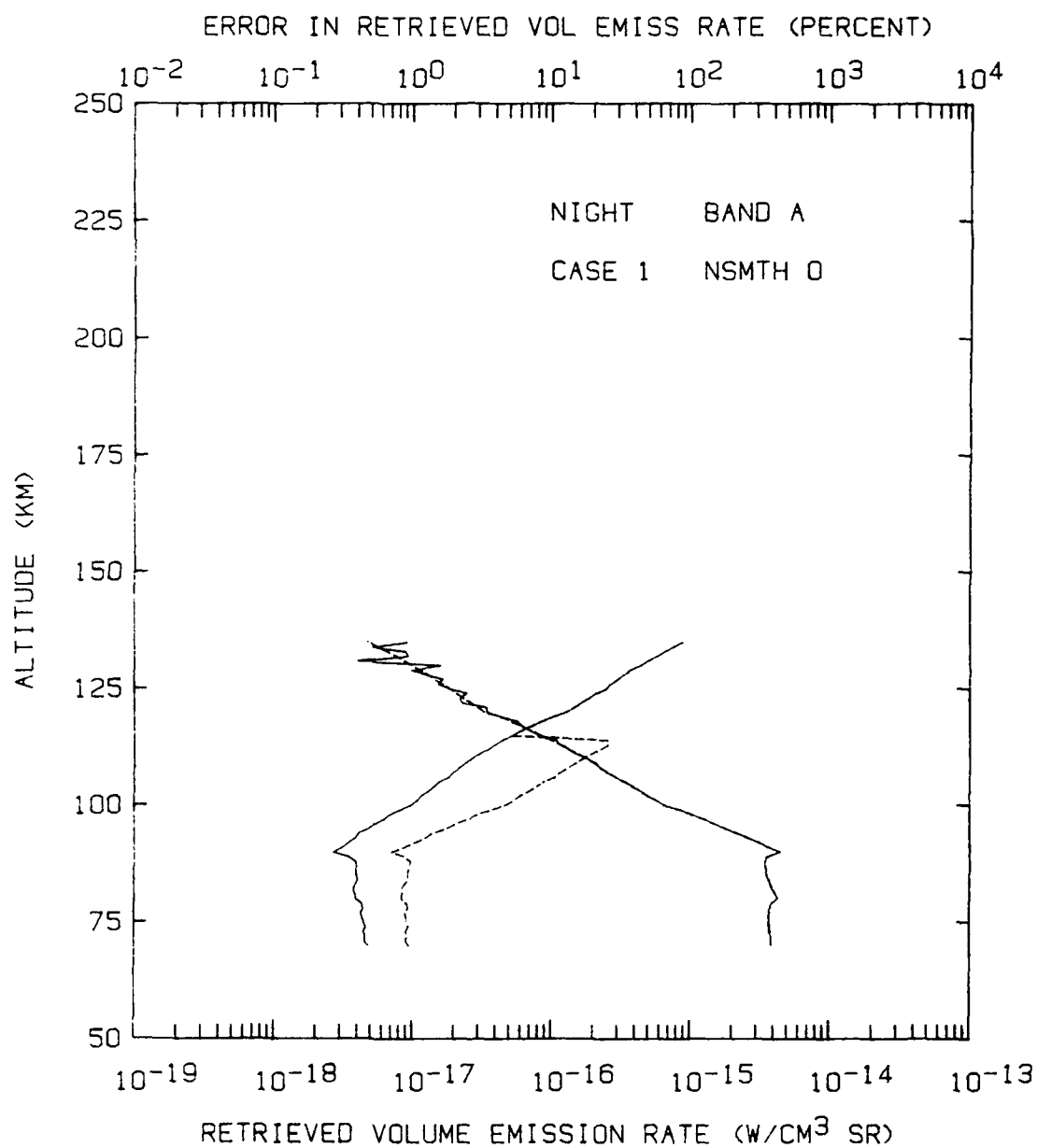


Figure 26. Same as Fig. 20, except the results represent Band A, Case 1.

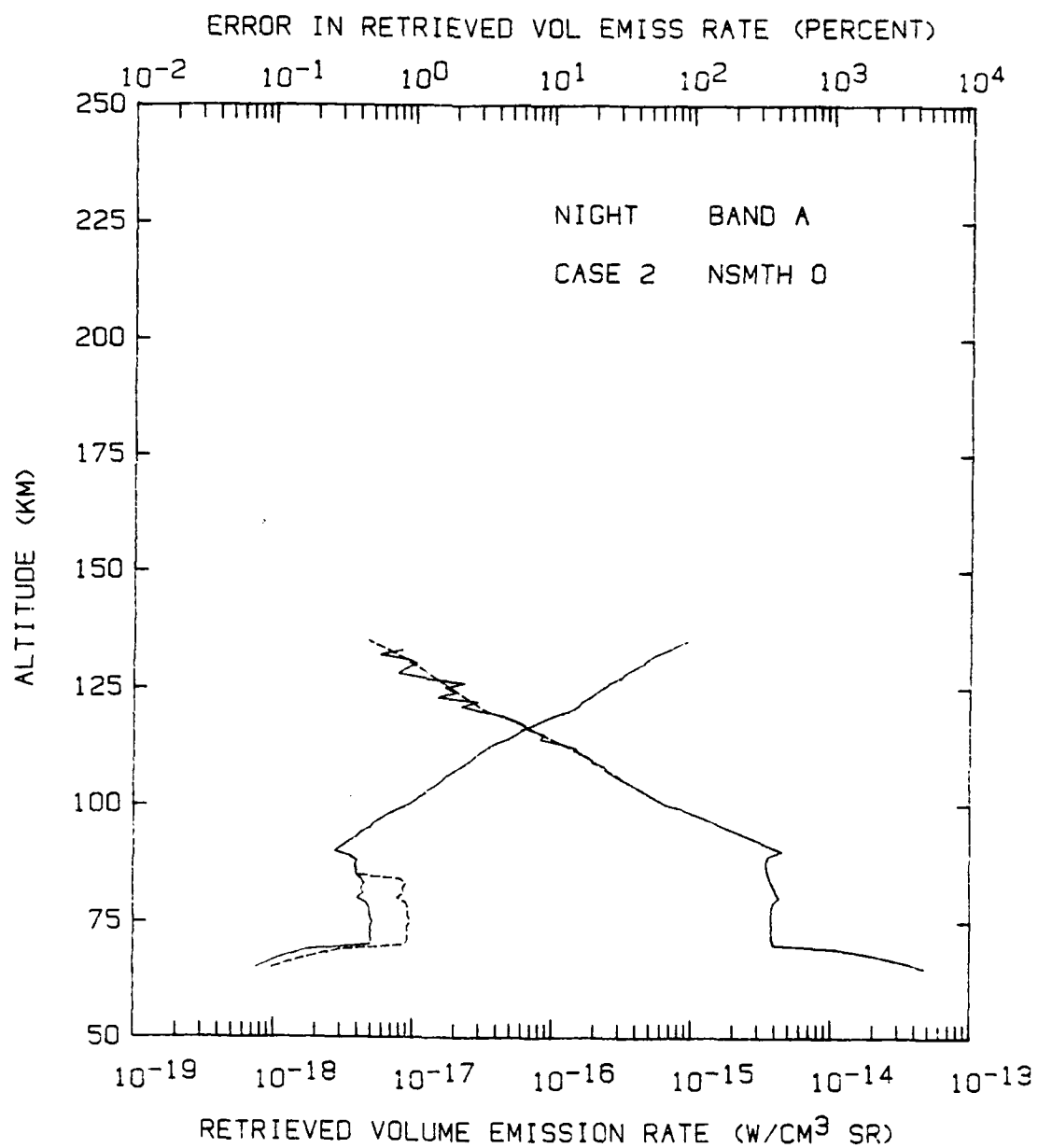


Figure 27. Same as Fig. 20, except the results represent Band A, Case 2.

SECTION 6

CONCLUSIONS

Section 2 and Appendix A describes a new inversion routine, based on a derivative-free form of the inverse Abel equation, that was used in the present study to estimate retrieval errors due to noise. Examination of the retrieval errors (in Sections 3.1 and 5.2) reveals an interesting fact: If the SNR of the limb radiance is of the order of 100 or less, the relative error in the retrieved density or volume emission rate is roughly seven times the NSR (noise-to-signal ratio)*. This factor-of-seven "noise amplification" by the inversion routine characterizes the inversion results for all altitude/tangent heights, ie., for all SNRs ≤ 100 .

Hansen and Law [1985] describe a recursive method for Abel inversion that, in the case of noisy data, provides the basis for an efficient least-squares estimation (Kalman filter) procedure. They compared their inversion procedure with two other stable techniques for Abel inversion: The method of Minerbo and Levy [1969] expands the data set in orthogonal (Hermite) polynomials, while Anderssen [1976] obtains an optimal estimate of the derivative in the Abel inverse equation through a Wiener filtering approach. Results obtained by Hansen and Law (H-L) indicate that the solutions obtained by all three methods have approximately the same level of error when the noise level is moderate (SNR ≈ 100) and provided the H-L method is used with a smoothing filter. We estimate that the error level is equivalent to a noise amplification factor of 0.7, which is ten times better than ours. However, the smoothing greatly

*In Section 5.2, the NSR of the synthetic SPIRIT 3 data was reduced by the factor $3.5^{1/2}$ to simulate one km vertical resolution. This factor was included in arriving at the factor-of-seven noise amplification.

reduces the resolution of the solution; it reduced the error in the tests by H-L only because the test cases (the equivalent of our volume emission rate profiles) were very smooth mathematical functions. It is possible that the other two methods also give solutions that are inherently smooth. When the H-L method is used without smoothing, the solutions have a noticeable bias error, and the noise amplification factor increases to about 4 to 7 for $SNR < 100$; ie., its performance without smoothing is roughly the same as the inversion routine used in the present study.

It is concluded from the results presented in Section 3.1 that a zenith-viewing rocket-borne instrument would require roughly 100 times greater sensitivity than a limb-viewing instrument to recover a volume emission rate profile to the same accuracy. This higher sensitivity can be achieved (for a given detector NEP) by using a larger IFOV; owing to photon noise it might be necessary to use a solid IFOV that is somewhat more than 100 times larger.

Horizontal variations in density caused by TIDs and thermospheric tidal or gravity wave perturbations are expected to result in retrieval errors no larger than 10 percent during quiet periods, and errors of perhaps 20 percent during geomagnetically active periods, as described in Section 3.2.

A number of conclusions regarding the performance of the SPIRIT 3 radiometer in Bands, D, E and A have already been stated in Section 5. Briefly, the SNRs based on SHARC limb radiance profiles are sufficiently high in Bands D and A to permit accurate limb radiance measurements, and reasonably accurate retrievals, of CO_2 and O_3 up to approximately 175 km and 125 km, respectively. Water vapor can be accurately recovered from the Band E data up to approximately 90 km altitude. Above 100 km the atmosphere is very dry, and the SNR above 100 km tangent height is

consequently very low (only 3.5) in Band E. This is a case where it would be desirable to use the Hansen and Law method of Kalman filter inversion with smoothing; it would allow retrieval of a low-resolution H_2O volume emission rate accurate to roughly 30 percent. It is emphasized that the inversion method used in the present study, or any method based on the Abel transform, is not strictly valid when self-absorption is important, which is probably the case for Band D at the lower tangent heights.

APPENDIX A

ROUTINES FOR THE ABEL TRANSFORM AND ITS INVERSE

Abel's integral equation

$$I(y) = 2 \int_y^{\mathfrak{R}} g(r) r (r^2 - y^2)^{-1/2} dr \quad (1)$$

can be used to obtain the limb radiance profile $I(y)$ corresponding to a given radial (altitude) distribution of volume emission rate $g(r)$, provided the limb viewing paths corresponding to all tangent heights y can be regarded as optically thin. The emission rate is assumed to be zero above $r = \mathfrak{R}$. Similarly, the emission rate profile $g(r)$ can be recovered, in the optically-thin case, from a given radiance profile $I(y)$ using the known inverse of Abel's equation:

$$g(r) = (-1/\pi) \int_r^{\mathfrak{R}} [dI(y)/dy] (y^2 - r^2)^{-1/2} dy \quad (2)$$

A measurement of $I(y)$ inevitably contains noise, which is greatly amplified by the derivative in Eq. (2).

Deutsch and Beniaminy [1982] were able to integrate Eq. (2) by parts to obtain an inversion formula that does not require differentiation of $I(y)$, and thus avoids amplification of error. Their formula is

$$g(r) = (-1/\pi) \{ [I(\mathfrak{R}) - I(r)] (\mathfrak{R}^2 - r^2)^{-1/2} + \int_r^{\mathfrak{R}} [I(y) - I(r)] y (y^2 - r^2)^{-3/2} dy \} \quad (3)$$

In the present study, the profiles $g(r)$ and $I(y)$ are each represented by piecewise linear distributions, that is, by a set of linearly connected samples. For these distributions it was possible to evaluate the integrals in Eqs. (1) and (3). The results are given by Eqs. (4) and (5), in which the position coordinate is now h , representing either tangent height or altitude above the earth's surface, rather than radial distance r from the earth's center:

$$I(h_j) = 2 \sum_{i=j}^{N-1} \left\{ g_i [{}^j Q_{i+1} - {}^j Q_i] + (c_i/2) [h_{i+1} - 2h_i - R] {}^j Q_{i+1} + (h_i + R) {}^j Q_i + (h_j + R)^2 \log((h_{i+1} + R + {}^j Q_{i+1}) / (h_i + R + {}^j Q_i)) \right\}; \quad (4)$$

$j = 1, 2, \dots, N-1; \quad I(h_N) = 0$

where $g_i = g(h_i); \quad i = 1, 2, \dots, N$

$R = \text{earth's radius} \approx 6371 \text{ km}$

$c_i = (g_{i+1} - g_i) / (h_{i+1} - h_i)$

${}^j Q_i = [(h_i - h_j)(2R + h_i + h_j)]^{1/2}$

$$g(h_i) = (1/\pi) \left\{ (I_i - I_N) / {}^i Q_N + d_i [(h_{i+1} - h_i) / {}^i Q_{i+1} - \log((h_{i+1} + R + {}^i Q_{i+1}) / (h_i + R))] + \sum_{j=i+1}^{N-1} \left\{ (I_j - I_i) (1 / {}^i Q_{j+1} - 1 / {}^i Q_j) + d_j [(h_{j+1} - h_j) / {}^i Q_{j+1} - \log((h_{j+1} + R + {}^i Q_{j+1}) / (h_j + R + {}^i Q_j))] \right\} \right\};$$

$i = 1, 2, \dots, N \quad (5)$

where $I_i = I(h_i)$

$d_i = (I_{i+1} - I_i) / (h_{i+1} - h_i)$

In these equations, \log denotes the natural logarithm. Note also that elements of the matrix J_{Q_i} are required only for $i \geq j$. The parameter d_j , defined below Eq. (5), is the numerical equivalent of the derivative of the limb radiance with respect to altitude, making it appear that Eq. (5) is not a derivative-free inverse solution. However, it can be demonstrated that the terms of Eq. (5) combine systematically, such that it is possible to obtain a formula (much longer than Eq. 5) that gives $g(h_i)$ as a weighted sum of the I_j rather than the d_j . In other words, Eq. (5), when evaluated, is indeed free of derivatives.

It should be noted that the assumption that the volume emission rate $g(h)$ is piecewise linear is not consistent with the assumption that the limb radiance profile $I(h)$ is also piecewise linear, and vice versa. That is, if one of the two profiles is represented by linearly connected samples, then the other profile, if it were obtained from an exact evaluation of the integral equation (1) or (3), would not have a linear variation between the sample points. Thus, if Eq. (4) is used to generate synthetic limb radiance values I_j from a given volume emission rate profile g_i , and then Eq. (5) is used to recover the g_i , the given and retrieved samples g_i will be systematically different. However, for the distributions involved in the present study the differences are less than 0.1 percent for a sample spacing of one km. By comparison, they are approximately one percent for a mesh size of two km. The error can be made as small as desired by decreasing the mesh size.

The computation of a limb radiance profile according to Eq. (4) can be carried out using subroutine FWD which is listed below. The argument VER is the name of the array containing NH volume emission rates $g(h_i)$, and the argument H is the array of corresponding altitudes h_i (which need not be uniformly spaced). The routine returns the limb radiance

profile $I(h_j)$ as array RAD. Similarly, an Abel limb inversion according to Eq. (5) can be performed by calling subroutine INV, also listed below. In this routine, RAD is the given limb radiance profile, and SOLN is the recovered volume emission rate vs. altitude. The calling program must supply to either routine the earth's radius R and the half-matrix Q containing the jQ_i for $i \geq j$. The latter can be created by calling subroutine GETQ.

```

      SUBROUTINE GETQ(NH,H,Q,R)
C*** COMPUTE HALF-MATRIX Q OF TANGENT PATH Z-DISTANCES.
C*** R IS RADIUS OF THE EARTH. GIVE R AND H VALUES IN KM.
      REAL H(NH), Q(NH,NH)
      DO 15 J=1,NH
      DO 15 I=J,NH
15   Q(I,J) = SQRT((H(I)-H(J))*(2.0*R+H(I)+H(J)))
      RETURN
      END

      SUBROUTINE FWD(NH,H,VER, RAD, Q,R)
C*** GIVEN THE VOLUME EMISSION RATE VER(I) VERSUS ALTITUDE
C*** H(I) FOR I = 1,...,NH, GET THE LIMB RADIANCE RAD(J)
C*** VERSUS TANGENT HEIGHT H(J) FOR J = 1,...,NH.
C*** Q IS HALF-MATRIX OF Z-DISTANCES (LENGTHS ALONG TANGENT
C*** PATH BETWEEN CONSECUTIVE ALTS H) AND R IS EARTH RADIUS
C*** -- BOTH (IN KM) ARE SUPPLIED BY THE CALLING PROGRAM.
C
C*** RAD IS OBTAINED BY EVALUATION OF THE ABEL INTEGRAL.
C*** THE INTEGRATION IS EXACT FOR LINEARLY CONNECTED VER
C*** VALUES. IF H IS IN KM, RAD WILL HAVE SAME UNITS AS VER
C*** TIMES CM.
C
      INTEGER H(NH)
      REAL VER(NH), RAD(NH), Q(NH,NH)
C
      DO 100 J=1,NH-1
      SUM = 0.0
      DO 50 I=J,NH-1
      C = (VER(I+1)-VER(I))/(H(I+1)-H(I))
      T1 = VER(I)*(Q(I+1,J)-Q(I,J))
      T21 = (H(I+1)-2.0*H(I)-R)*Q(I+1,J)
      T22 = (H(I)+R)*Q(I,J)
      T23 = (H(J)+R)**2*ALOG((H(I+1)+R+Q(I+1,J))/
$                               (H(I)+R+Q(I,J)))
50   SUM = SUM + T1 + (T21+T22+T23)*C/2.0
100  RAD(J) = SUM*2.0E+5
      RAD(NH) = 0.0
      RETURN
      END

```

```

      SUBROUTINE INV(NH,H,RAD, SOLN, Q,R)
C*** GIVEN A LIMB RADIANCE PROFILE RAD(J) VS. TANG. HT.
C*** H(J) FOR J = 1,...,NH, RETRIEVE THE VOLUME EMISSION
C*** RATE SOLN(I) VS. ALTITUDE H(I) FOR I = 1,...,NH.
C*** Q IS HALF-MATRIX OF Z-DISTANCES AND R IS EARTH RADIUS
C*** -- BOTH (IN KM) ARE SUPPLIED BY THE CALLING PROGRAM.
C*** SOLN HAS THE UNITS OF RAD TIMES 1/CM.
C
C*** SOLN IS OBTAINED BY EVALUATION OF A DERIVATIVE-FREE
C*** FORM OF THE INVERSE ABLE INTEGRAL EQUATION -- SEE
C*** DEUTSCH AND BENIAMINY, APPL. PHYS. LETT., VOL 41, P. 27
C*** (JULY, 1982). THE INTEGRATION PERFORMED HERE
C*** IS EXACT FOR LINEARLY CONNECTED RAD VALUES.
C
      INTEGER H(NH)
      REAL RAD(NH), SOLN(NH), Q(NH,NH)
C
      PARAMETER( CONS = 314159.26536 )
C*** CONS IS PI TIMES 1.E5 CM/KM
C
      DO 100 I=1,NH-1
        C = (RAD(I+1)-RAD(I))/(H(I+1)-H(I))
        T1 = (RAD(I)-RAD(NH))/Q(NH,I)
        T21 = (H(I+1)-H(I))/Q(I+1,I)
        T22 = ALOG((H(I+1)+R+Q(I+1,I))/(H(I)+R))
        SUM = T1 + (T21-T22)*C
        DO 50 J=I+1,NH-1
          C = (RAD(J+1)-RAD(J))/(H(J+1)-H(J))
          T1 = (RAD(J)-RAD(I))*(1.0/Q(J+1,I) - 1.0/Q(J,I))
          T21 = (H(J+1)-H(J))/Q(J+1,I)
          T22 = ALOG((H(J+1)+R+Q(J+1,I))/(H(J)+R+Q(J,I)))
50      SUM = SUM + T1 + (T21-T22)*C
100    SOLN(I) = SUM/CONS
      RETURN
      END

```

APPENDIX B

FILES AND EXECUTION PROCEDURES FOR THE CYBER VERSION OF THE SHARC CODE

Tape CC0888 in the GL tape library contains a complete set of files that can be used to compile and/or execute the Cyber version of SHARC under the NOS operating system. This is a RECLAIM tape, i.e., it was created using the DUMP directive of RECLAIM, a utility program for dumping or loading permanent files on the NOS system. RECLAIM can be used to load files from Tape CC0888 to the Cyber system, as needed.

Table B.1 is a listing of the tape, i.e., a list of the file names, their lengths, etc., produced by RECLAIM. The files include all of the SHARC modules (modified source code), an executable object file of the compiled modules, the various data files required by SHARC, and a sample batch file, consisting of commands liberally interspersed with comments, to run SHARC in the batch mode. Users familiar with SHARC will recognize many of the file names in Table B.1.

Table B.1 Listing of tape CC0888 (Edited RECLAIM listing)

PFN	TYPE	LAST MOD	DUMP DATE	LENGTH	FI	REC
ASCI	I	89/03/20	89/04/27	3	1	8
BINARY	I	89/03/14	89/04/27	3	1	47
BINCHRC	D	89/04/20	89/04/27	627	1	3
CHEMKIN	I	89/04/05	89/04/27	58	1	40
COBAND	I	89/03/13	89/04/27	4	1	23
COKIN	I	89/03/13	89/04/27	5	1	49
COLINK	I	89/04/06	89/04/27	18	1	13
CONVSHC	I	89/04/19	89/04/27	8	1	11
COOUT	I	89/03/14	89/04/27	6	1	64
COSTAT	I	89/03/13	89/04/27	2	1	18
CO2BAND	I	89/03/13	89/04/27	27	1	25
CO2KIN	I	89/03/13	89/04/27	27	1	48
CO2LINK	I	89/04/06	89/04/27	119	1	15
CO2OUT	I	89/03/14	89/04/27	30	1	63
CO2STAT	I	89/03/13	89/04/27	4	1	20
DUMPSHC	I	89/04/27	89/04/27	3	1	12

Table B.1 (Continued)

FTNSHRC	I	89/04/10	89/04/27	2	1	5
GEOMTRY	I	89/04/14	89/04/27	53	1	41
H2OBAND	I	89/03/13	89/04/27	13	1	26
H2OKIN	I	89/03/13	89/04/27	10	1	50
H2OLINK	I	89/04/06	89/04/27	40	1	16
H2OOUT	I	89/03/14	89/04/27	11	1	65
H2OSTAT	I	89/03/13	89/04/27	3	1	21
INSUBS	I	89/04/15	89/04/27	214	1	42
INTERP	I	89/04/05	89/04/27	133	1	46
MAKSML	I	89/03/20	89/04/27	2	1	7
MAKSMLL	I	89/03/14	89/04/27	4	1	6
NEMESIS	I	89/04/07	89/04/27	60	1	43
NOBAND	I	89/03/13	89/04/27	4	1	24
NOKIN	I	89/03/13	89/04/27	4	1	51
NOLINK	I	89/04/06	89/04/27	16	1	14
NOOUT	I	89/03/14	89/04/27	5	1	66
NOSTAT	I	89/03/13	89/04/27	2	1	19
OUTSUBS	I	89/04/15	89/04/27	63	1	44
O3BAND	I	89/03/13	89/04/27	21	1	27
O3KIN	I	89/03/13	89/04/27	21	1	52
O3LINK	I	89/04/06	89/04/27	86	1	17
O3OUT	I	89/03/14	89/04/27	26	1	67
O3STAT	I	89/03/13	89/04/27	4	1	22
PO1976N	I	89/04/15	89/04/27	259	1	29
RDM8476	I	89/03/13	89/04/27	10	1	10
RD8476	I	89/03/14	89/04/27	4	1	9
RNSHARC	I	89/04/20	89/04/27	3	1	2
RUNSHRC	I	89/04/15	89/04/27	2	1	1
SAT15AN	I	89/04/10	89/04/27	83	1	31
SAT1976	I	89/04/10	89/04/27	29	1	30
SAT30SM	I	89/04/10	89/04/27	83	1	32
SAT30WN	I	89/04/10	89/04/27	83	1	33
SAT45SM	I	89/04/10	89/04/27	83	1	35
SAT45SP	I	89/04/10	89/04/27	83	1	34
SAT45WN	I	89/04/10	89/04/27	83	1	36
SAT60SM	I	89/04/10	89/04/27	83	1	37
SAT60WN	I	89/04/10	89/04/27	83	1	38
SHARC	I	89/04/14	89/04/27	40	1	39
SHARCIN	I	89/04/10	89/04/27	10	1	53
SHARC1I	I	89/04/10	89/04/27	10	1	54
SHARC1O	I	89/03/14	89/04/27	153	1	57
SHARC1S	I	89/03/14	89/04/27	285	1	60
SHARC2I	I	89/04/10	89/04/27	10	1	55
SHARC2O	I	89/03/14	89/04/27	145	1	58
SHARC2S	I	89/03/14	89/04/27	29	1	61
SHARC3I	I	89/04/10	89/04/27	10	1	56
SHARC3O	I	89/03/14	89/04/27	11	1	59
SHARC3S	I	89/03/14	89/04/27	29	1	62
SHCIN2	I	89/04/15	89/04/27	2	1	28
SMALLER	D	89/04/05	89/04/27	10500	1	4
SPCTRA	I	89/04/14	89/04/27	64	1	45

The following simple procedure can be used to execute SHARC on the Cyber from the object code file BINSHRC:

1. Use RECLAIM to load the file RNSHARC from tape CC0888. This is a prototype ASCII batch file containing a sequence of NOS commands to run SHARC in its batch mode.
2. Examine RNSHARC, ie., a screen display or printout, and load all files referenced in GET and ATTACH commands. This will include the executable file BINSHRC, various data files, and a file of input directives for SHARC. Comment lines in RNSHARC indicate the commands and file names that can be changed to effect different modes of operation and to vary user choices. It is assumed that the user is familiar with the NOS system commands and with the general input/output procedures used by SHARC, as described in the SHARC documentation [Sharma, et al. 1989]. The user should use his/her User Name (UN) when loading the files and replace ZACHOR by that UN in the GET and ATTACH commands (or remove the /UN=ZACHOR).
3. After modifying RNSHARC as necessary, submit it as a NOS batch job. The SHARC outputs will be found in the permanent files referenced in REPLACE and DEFINE commands in RNSHARC ;if not renamed, these are POPNEW, SHCER2, SHCSPC2 and SHCOUT2.

The line parameter file attached by RNSHARC is SMALLER, an abbreviated version of the original line file for SHARC. Use of this file reduces the range over which radiances can be computed from the original 2-40 μm to 5-27 μm . However, it is possible to overcome this restriction, as described below.

The Cyber version of SHARC reads line parameters from an ASCII file, unlike the Apollo version, which reads a binary line file. The ASCII file is long, but a binary version on the Cyber would be considerably longer due to the long (60-bit) word length of the Cyber; on the Apollo the binary version is shorter than the ASCII version. File SMALLER requires 10,500 PRUs of permanent storage, a rather large amount on the Cyber system. Its 5-27 μm spectral

range is adequate for modelling radiances in the SPIRIT 3 bands.

Files MAKXML and ASCII on tape CC0888 provide a means of creating a new ASCII line file (a new version of SMALLER) that covers any subinterval of the 2-40 μm region. MAKXML is a batch file that loads the original line file (the full-length ASCII version supplied by SSI to GL), and then compiles and executes Fortran program ASCII to create an abbreviated version. The PARAMETER statement in ASCII determines the spectral range of the created line file.

The batch file FTNSHRC can be used to recompile the SHARC source code modules should future modifications be necessary. This file was used to create BINSHRC. The object code produced by FTNSHRC requires use of the Cyber's extended core storage (ECS). The batch file DUMPSHC was used to dump all permanent files listed in Table B.1 to tape CC0888. The Fortran code CONVSHC can be used to convolve a SHARC spectrum with a sinc or sinc-squared instrumental line shape, representative of an interferometer.

The files in Table B.1 that have not been mentioned by name include the modified SHARC modules, the many data files required by SHARC (which have not been modified), "linking" and "population" files computed on the Cyber, and sample input/output files. Many of the original file names had to be changed since the NOS system does not support name extensions or names longer than seven characters. Table B.2 lists the changes. The last three entries are the temporary local file names used by the modified Interpreter program (module INTERP) to create the linking files for each molecular radiator.

Access to the Cyber version of the SHARC requires authorization from the Geophysics Laboratory (Dr. Ramesh Sharma, GL/OP) at Hanscom AFB.

Table B.2 Renamed SHARC files

<u>Apollo</u>	<u>Cyber</u>
INPUT	INSUBS
OUTPUT	OUTSUBS
().DAT	()
SHARC.INP	SHARCIN
LINE.ASC	SMALLER (5-27 μ m only)
SHARC*.INP	SHARC*I (* = 1, 2 or 3)
SHARC*.OUT	SHARC*O (* = 1, 2 or 3)
SHARC*.SPC	SHARC*S (* = 1, 2 or 3)
SHARC.ERR	SHARCER

INTERP.INP	INTRPIN
INTERP.OUT	INTRPOU
INTERP.LNK	INTRPLN

REFERENCES

- R. S. Andersen [1976], "Stable procedures for the inversion of Abel's equation," *J. Inst. Math. Its Appl.* **17**, 329-342.
- M. Deutsch and I. Beniaminy [1982], "Derivative-free inversion of Abel's integral equation," *Appl. Phys. Lett.* **41**, 27-28.
- J. M. Forbes, F. A. Marcos and P. F. Fougere [1987], "Wave structures in thermospheric density from satellite electrostatic triaxial accelerometer measurements," AFGL-TR-87-0189, Air Force Geophysics Laboratory, Hanscom AFB, MA 01731. ADA194134
- B. F. Gordiets, Y. M. Kulikov, M. N. Markov and M. Y. Marov [1982], "Numerical modeling of the thermospheric heat budget," *J. Geophys. Res.*, **87**, 4504.
- E. W. Hansen and P.-L. Law [1985], "Recursive methods for computing the Abel transform and its Inverse," *J. Opt. Soc. Am. A* **2**, 510-520.
- T. L. Killeen and R. G. Roble [1988], "Thermospheric dynamics: contributions from the first 5 years of the Dynamic Explorer Program," *Rev. Geophys.* **26**, 329-367.
- G. N. Minerbo and M. E. Levy [1969], "Inversion of Abel's integral equation by means of orthogonal polynomials," *SIAM J. Numer. Anal.* **6**, 598-616.
- A. Savitzky and M. J. E. Golay [1964], "Smoothing and differentiation of data by simplified least squares procedures; *Anal. Chem.* **36**, 1627-1639. Some corrections to tables in this paper are given by Steinier et al, *Anal. Chem.* **44**, 1906 [1972].
- R. D. Sharma, A. J. Ratkowski, R. L. Sundberg, J. W. Duff, L. S. Bernstein, P. K. Acharya, J. H. Gruninger and D. C. Robertson [1989], "The Strategic High-altitude Atmospheric Radiation Code (SHARC) user instructions," AFGL-TR-89-0062, Air Force Geophysics Laboratory, Hanscom AFB, MA 01730-5000. ADA207667
- A. S. Zachor, R. D. Sharma, R. M. Nadile and A. T. Stair, Jr. [1985], "Inversion of a spectrally resolved limb radiance profile for the NO fundamental band," *J. Geophys. Res.* **90**, 9776-9782.